Ph.D. Dissertation of Science

Oceanic response to changes in wind and surface heating off the southern coast of the Korean Peninsula

한반도 남해안에서 바람과 표층 가열의 변화에 대한 해양의 반응

February 2023

School of Earth and Environmental Sciences
Graduate School
Seoul National University

Jihun Jung

Oceanic response to changes in wind and surface heating off the southern coast of the Korean Peninsula

Supervisor: Yang-Ki Cho, Professor

Submitting a Ph.D. Dissertation of Science
October 2022

School of Earth and Environmental Sciences
Graduate School
Seoul National University
Jihun Jung

Confirming the Ph.D. Dissertation written by
Jihun Jung
January 2023

Chair	Sung-Hyun Nam	(Seal)
Vice Chair	Yang-Ki Cho	(Seal)
Examiner	Hanna Na	(Seal)
Examiner	Byoung-Ju Choi	(Seal)
Examiner	Young Ho Kim	(Seal)

Abstract

The oceanic response to changes in wind and surface heating off the southern coast of the Korean Peninsula was investigated.

Unprecedented coastal upwelling off the southern coast of the Korean Peninsula was reported during the summer of 2013. The upwelling continued for more than a month after a plunge in upwelling-favourable winds and had serious impacts on fisheries. Coastal upwelling was induced by an upwelling-favourable wind in July, resulting in the dynamic uplift of deep, cold water. The dynamic uplift decreased the steric sea level in the coastal region. The sea level difference between the coastal and offshore regions produced an intensified cross-shore pressure gradient that enhanced the surface geostrophic current along the coast. The strong surface current maintained the dynamic uplift due to geostrophic equilibrium. This positive feedback between the dynamic uplift and geostrophic adjustment sustained the coastal upwelling for a month following a plunge in the upwelling-favourable wind.

Numerical experiments were conducted to evaluate the effects of surface heating on coastal upwelling intensity. Offshore transport, isopycnal slope, and the sea surface temperature (SST) difference

between coastal and offshore regions, which represent the upwelling intensity, were estimated. Surface heating decreases Ekman transport but increases Ekman pumping by changing air–sea stability conditions. However, offshore transport does not change significantly with surface heating. Experimental results revealed that the increase in surface heating decreases the isopycnal slope but increases the SST difference. Both the isopycnal slope and SST difference are closely related to the change in the surface boundary layer. Strong surface heating thins the surface–mixed layer, which decreases the vertical eddy viscosity. The decreased vertical eddy viscosity thins the surface boundary layer and enhances its offshore velocity. Despite the same offshore transport, the isopycnal slope weakens because of the thin surface boundary layer, while the SST difference becomes stronger because of the enhanced offshore velocity.

Coastal wind–driven asymmetric response of the alongshore surface currents over a bank was observed in 2019. The alongshore currents displayed greater variability over the upstream part of the bank than those over the downstream. The main cause of this asymmetry is the difference in ageostrophic motion, which depends on the depth–averaged surface stress. The asymmetric distribution of sea level induced by the difference in ageostrophic motion resulted

in larger variability in the alongshore currents over the upstream part of the bank. Offshore currents have a significant impact on the alongshore currents and sea level distribution over the bank. In the case of easterly winds, the westward currents linger and propagate over the upstream part of the bank in the eastward direction. The sea level distribution shows a minimum sea level near the bank head. On the other hand, in the case of westerly winds, the offshore currents intensify the asymmetry in alongshore currents and sea level distribution.

Keyword : Southern coast of the Korean Peninsula, Oceanic response, Wind, Surface heating
Student Number : 2014-21314

Table of Contents

List of Figures

List of Tables

1. General Introduction

The coastal sea off the south coast of Korea is surrounded by the East Sea, East China Sea, and Yellow Sea. This region is located at the southern boundary of the East Sea (Byun and Choi, 2018). The southern coast has a complex coastline and topography with a mean depth of approximately 100 m (Fig. 1.1).

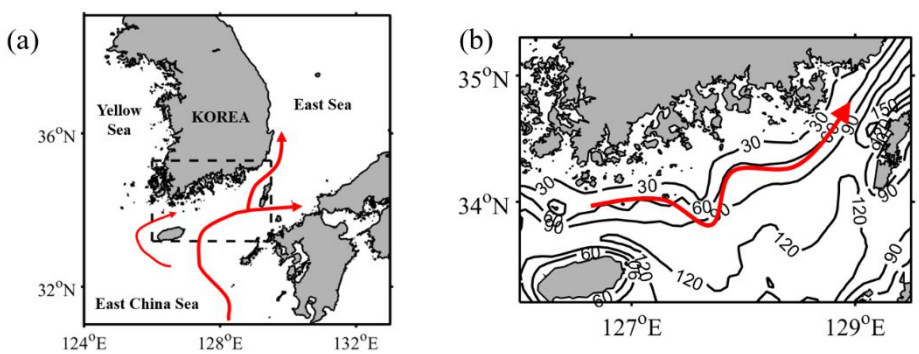

Figure 1.1 Study area (black dashed rectangle in Fig. 1.1a and 1.1b) with isobaths shown in meter. Red arrows represent a schematic of offshore currents.

In the early 1900s, general characteristics of the waters off the southern coast of the Korean Peninsula were described (Nishida, 1926; Uda, 1934). Since then, many studies have been conducted to investigate the characteristics of water masses and circulation. Water

masses off the southern coast of the Korean Peninsula exhibit strong seasonal variations (Gong, 1971; Kang, 1974; Lim, 1976). It was previously established that the coastal water mass formed in winter remains in the coastal region throughout the year. However, Cho and Kim (1994) and Cho et al. (1995) revealed that the bottom cold water in the summer flows into the area from neighboring seas, and the origin of the cold water is west of the Cheju Strait. Results of currents observation near the southern coastal region supported this theory (Pang et al., 2003; Teague et al., 2003). A recent research suggested that cold water is formed by the mixing of the Yellow Sea Bottom Cold Water (YSBCW) and the Tsushima Warm Current in the northern East China Sea region (Kim et al., 2022).

Circulation in the southern coastal region of the Korean Peninsula is strongly affected by the Tsushima Current (Gong, 1971; Kang, 1974; Lie and Cho, 2016; Seung, 1992). The flow path of the Tsushima Current is deflected by the effect of topography (Kim et al., 2000). Because the Tsushima Current has a high temperature and salinity, a strong front forms between the coastal region and the path of the Tsushima Current (Gong, 1971; Kang, 1974; Lee et al., 2018). In the summer, less saline surface water originating from China's coastal region flows into the southern coastal region through the

Cheju Strait (Kim and Rho, 1994). Several numerical modeling studies have been conducted to understand the general features of circulation in the southern coastal region (Bae and Kim, 2012; Kim et al., 2000; Kwoun et al., 2002).

Although previous studies have revealed some characteristics of water masses and circulation in the study area, the lack of observations and oversimplified numerical model experiments preclude the understanding of oceanic responses to realistic forcing and the underlying dynamics.

The most distinguishable cause of coastal circulation is alongshore wind stress (Allen, 1980). The alongshore wind stress causes upwelling or downwelling. Coastal upwelling can result in the transport of nutrient-rich, deep, cold water from greater depths to the surface euphotic zone, which affects coastal ecosystems. In addition, the onshore-offshore transport induced by the alongshore wind stress can excite coastal-trapped waves (Allen, 1980; Brink, 1991) which affect alongshore coastal currents (Park and Nam, 2018) and subtidal sea level fluctuations (Lee et al., 2022) around the Korean Peninsula.

Surface heating, combined with alongshore wind stress, can modulate wind-driven coastal circulation by changing water column

stratification (Allen et al., 1995; Lentz, 2001). Since the 1970s, the air temperatures in the study area have increased continuously (Fig. 1.2). Increasing air temperature may result in strong stratification, which modulates wind-driven coastal circulation.

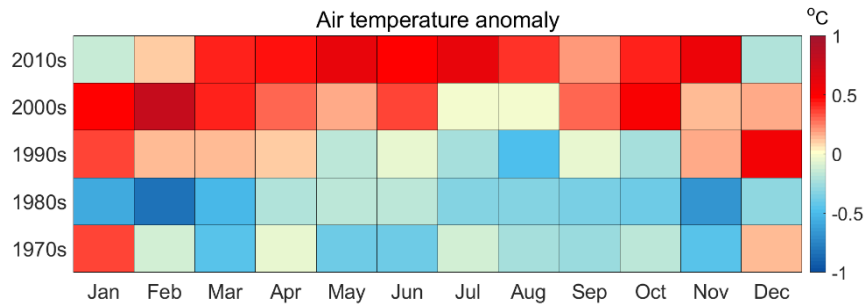

Figure 1.2 Monthly mean of air temperature anomaly averaged over the study area (Fig. 1.1b) calculated from ECMWF ERA5.

The combined effects of wind and surface heating influence not only the coastal environment but also coastal ecosystems. In the summer of 2013, for example, unprecedented harmful algal blooms were reported along the southern coast of the Korean Peninsula. The first outbreak was the earliest, and the total loss was estimated to be 24.7 billion won (the second largest). The National Institute of Fisheries Science suggested that the main causes of unprecedented harmful algal blooms were high air temperatures and persistent strong winds in July 2013. While the predominant wind over the

Yellow Sea was southerly, which extends the southern limit of the YSBCW (Yang et al., 2014), the predominant wind over the coastal sea off the south coast of Korea was southwesterly, which can cause coastal upwelling along the coast. In the future, the southern coast of the Korean Peninsula will be more exposed to strong surface heating conditions due to global climate changes. Harmful algal blooms resulting from the combined effects of wind and strong surface heating may occur frequently under future global warming scenarios. Despite the importance of understanding the oceanic response to changes in wind and surface heating off the southern coast of the Korean Peninsula, it still remains a subject for inquiry.

2. Persistence of coastal upwelling after a plunge in upwelling–favourable wind[①]

2.1. Introduction

Coastal upwelling is a process that brings deep, cold water to the ocean surface. It can play an important role both in physical processes and in chemical and biological variability in coastal regions by transporting nutrients to the surface layer. Coastal upwelling can be induced by various mechanisms, but it generally results from Ekman transport due to the alongshore wind stress (Ekman, 1905; Shi et al., 2000). Wind stress curl can also induce coastal upwelling (Castelao and Barth, 2006a). The current along a coastal region may enhance the onshore Ekman pumping through the bottom boundary layer (Roughan and Middleton, 2004; Roughan et al., 2003). Upwelling occurs as a form of dynamic (isotherm) uplift that results from geostrophic equilibrium, which is a balance between the pressure gradient force (PGF) and the Coriolis force (Kämpf and Chapman, 2016; Shen et al., 2011).

The southern sea region off the Korean Peninsula connects the

① The results of the presented work have been published in Jung and Cho (2020).

East China Sea and the East/Japan Sea. The mean depth of this offshore region is approximately 100 m. There is an eastward alongshore flow throughout the year (Pang et al., 2003; Teague et al., 2003). A two-layer structure, comprising warm water in the upper layer and cold water in the lower layer, forms during the summer. The surface waters that originate from the Kuroshio and East China Sea are heated by the atmosphere. The deep, cold water originates from the west (Cho and Kim, 1994; Cho et al., 1995).

Unprecedented coastal upwelling was reported in various observations during August 2013. The sea surface temperature (SST) in the coastal region was 2 ° C lower than the climatic SST (10 years mean) in the coastal region, whereas the offshore SST was 2 ° C higher due to a hot summer in 2013 (Fig. 2.1c). The cold SST in the coastal region persisted for more than a month after the upwelling-favourable wind weakened (Fig. 2.1e). The upwelling had serious impacts on the fish farms in this area.

In this study, observational data analyses and numerical modelling were performed to investigate the reason for the unprecedented coastal upwelling, as well as why it was sustained for such an extended period on the southern coast of the Korean Peninsula during the summer of 2013.

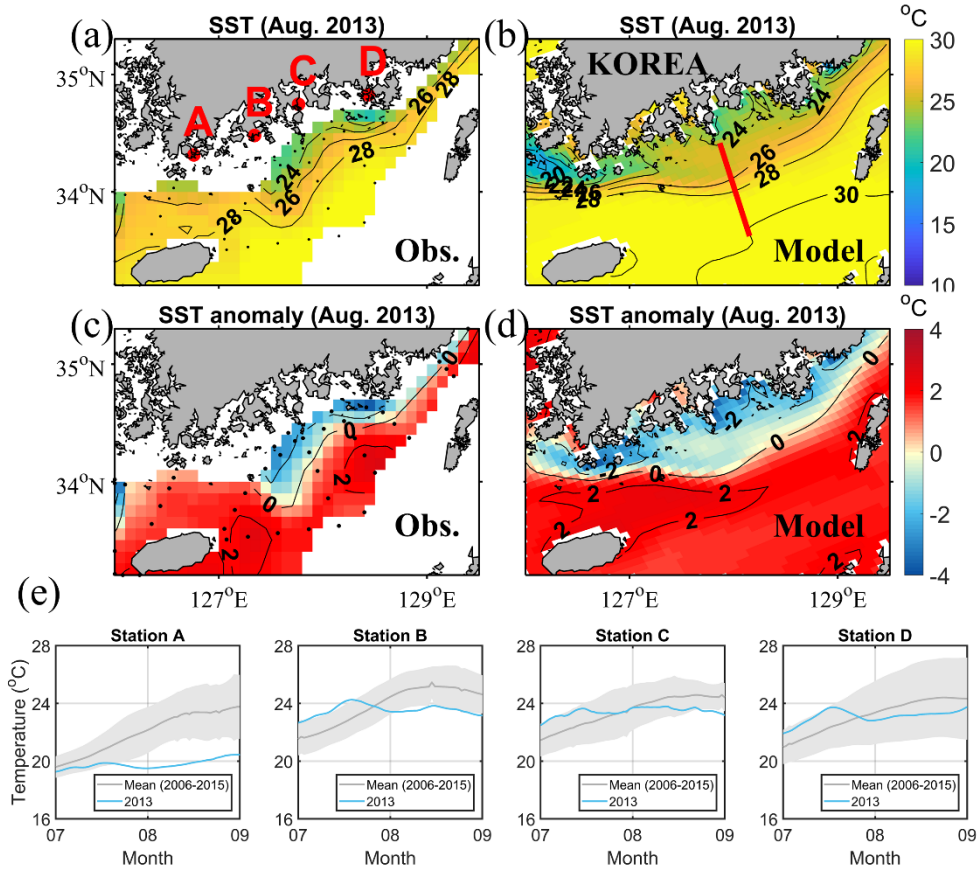

Figure 2.1 Monthly mean sea surface temperatures (SST) during August 2013 from (a) observations (Obs.) and (b) model results. The 10 years SST anomaly during August 2013 from (c) observations and (d) model results. (e) Time series of the 2-week running mean SST during 2013 (blue) and the 10 years mean with standard deviation (grey shadow) at tidal stations A–D (red dots in a). Black dots in (a) and (c) indicate the observation stations.

2.2. Results

2.2.1. Unprecedented coastal upwelling

The SST and its anomaly during August 2013 from observational data and model results are shown in Fig. 2.1. The anomaly was calculated from the 10 years mean SST value (2006-2015). The water temperature near the coastal region was ~ 5 ° C lower than the offshore water temperature commonly observed in both observational and modelled data (Figs. 2.1a and 2.1b). This relatively large temperature difference between the coastal and offshore regions was unprecedented. The SST anomaly was remarkable because the water temperature in the coastal region was 2 ° C lower than the climatic SST, whereas the offshore water temperature was 2 ° C higher (Figs. 2.1c and 2.1d). The positive offshore anomaly was the result of a hot summer in 2013. Despite the positive offshore anomaly, the negative coastal anomaly suggests that there was active coastal upwelling during the summer of 2013. Time series of temperature data from four tidal stations along the coast are shown in Fig. 2.1e. The 2-week running mean SST during 2013 was similar to, or higher than, the 10 years mean for July, but was lower than the

10 years mean at all stations during August. This also implies that there was strong coastal upwelling during August.

Monthly mean vertical cross sections along the red line in Fig. 2.1b are shown in Fig. 2.2. The temperature sections (Figs. 2.2a and 2.2c) show that the isotherms rose in the coastal region, indicating that upwelling occurred during both July and August. The slope of the isotherms in August was steeper than in July. The alongshore velocity sections (Figs. 2.2b and 2.2d) demonstrate that the surface alongshore velocity was higher in August than in July, while the bottom velocity was similarly weak. This suggests that the upwelling was stronger, and the vertical velocity shear was larger in August than in July. The increased vertical velocity shear induced a dynamic uplift of the isotherms that resulted from the geostrophic adjustment between the upper and lower layers in August.

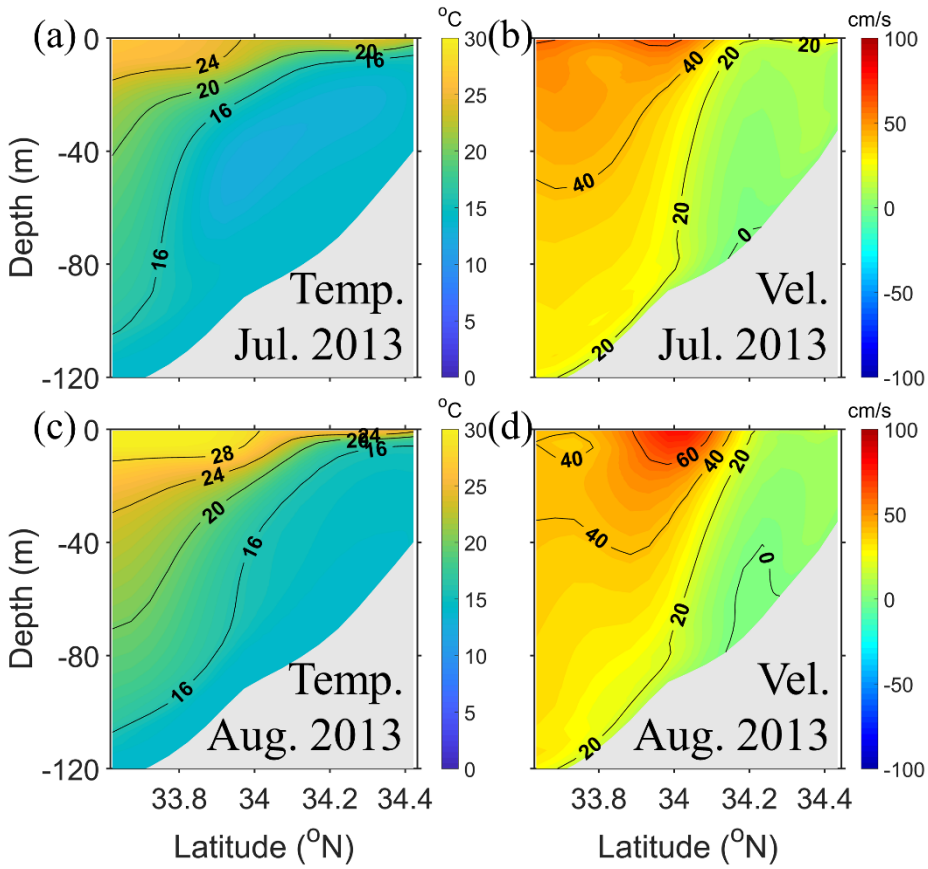

Figure 2.2 Model calculated cross-shore sections of the monthly mean temperatures (Temp., left) and alongshore velocities (Vel., right) during July (a, b) and August (c, d) along the red line in Fig. 2.1b.

2.2.2. Momentum balances

Monthly mean alongshore and cross-shore momentum balances in the cross section along the red line in Fig. 2.1b were analysed to investigate the cause of the upwelling (Fig. 2.3). Figs. 2.3a and 2.3b

illustrate the alongshore momentum terms for July and August, respectively. In July, the vertical viscosity at the surface was balanced with the Coriolis force, which suggests that Ekman transport was induced by the surface alongshore wind-stress. However, the vertical viscosity at the surface was very small in August, compared to July. The Coriolis force and the vertical viscosity at the bottom were balanced in both July and August, indicating the presence of a bottom Ekman layer. The magnitudes of the bottom Ekman layer were similar in July and August. The PGF was balanced with the Coriolis force in the interior region in both July and August.

The PGF and the Coriolis force were remarkable in the cross-shore momentum balance in July and August (Figs. 2.3c and 2.3d). The barotropic pressure gradient induced by the surface slope was larger in August than in July. The pressure gradient in the lower layer decreased due to the baroclinic pressure gradient caused by the dynamic uplift, which resulted in a slow current in the lower layer. The vertical viscosity in the cross-shore momentum balance was relatively small during both months.

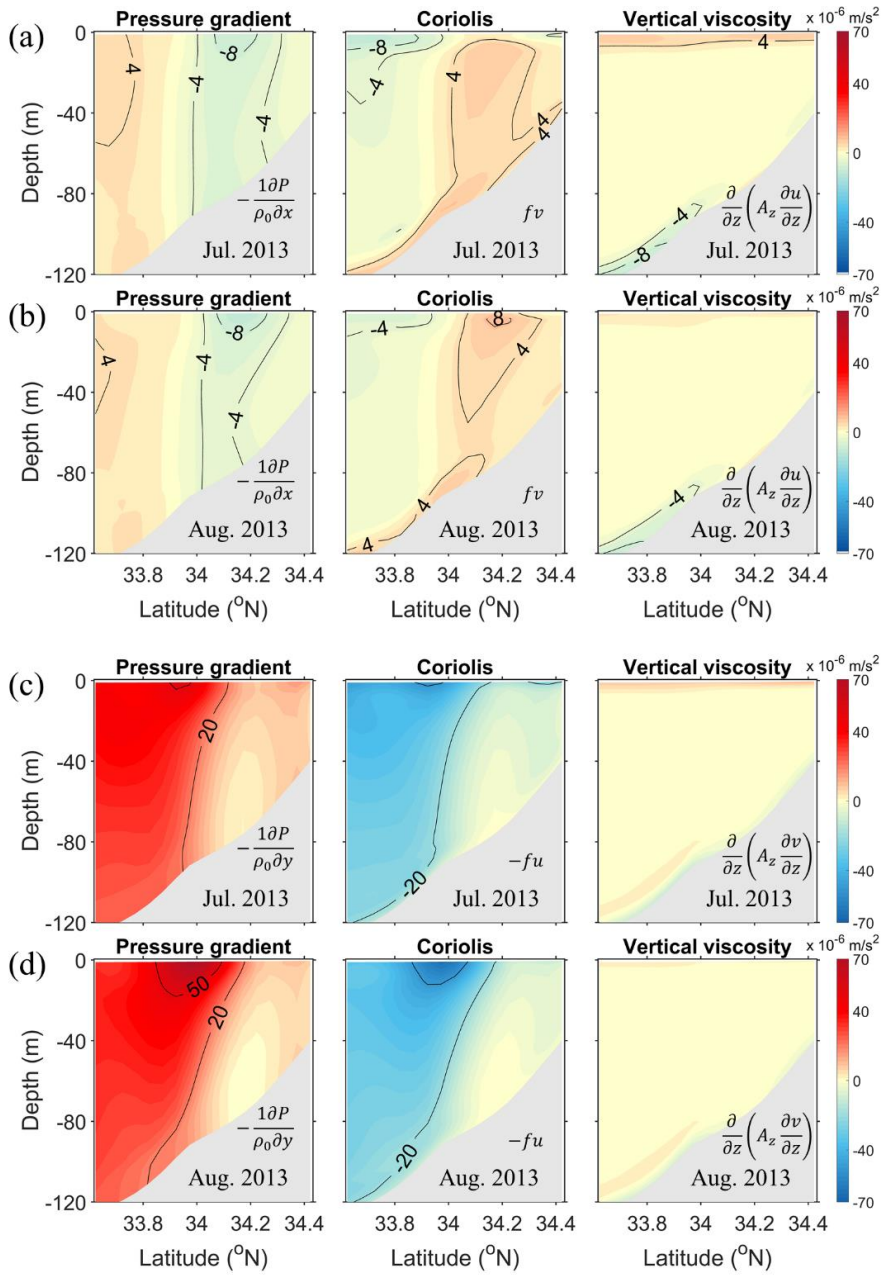

Figure 2.3 Monthly means of the alongshore momentum balance terms from the model results for (a) July and (b) August along the red line in Fig. 2.1b. Monthly means of the cross-shore momentum balance terms for (c) July and (d) August along the red line in Fig. 2.1b.

A time series of the momentum balance in the coastal and offshore regions (red dots in Fig. A1) show the evolution of the momentum balance after the weakening of the wind stress. The PGF and Coriolis force increased gradually in the cross-shore direction, while the vertical viscosity at the surface decreased rapidly in the alongshore direction, according to the weakening of the wind stress in early August (Figs. A2 and A3).

2.2.3. Temporal variations in the upwelling index and causes that drive upwelling

To examine the relationship between the upwelling strength and its possible causes, the upwelling index (UI), the wind-driven upwelling transport, the Ekman pumping transport, the slope of the interface representing dynamic uplift, and the sea level difference between the coastal and offshore regions were calculated.

The UI increased rapidly in mid-July and reached its maximum in late July (Fig. 2.4a). This corresponded with the temporal variations in temperature observed at the tidal stations (Fig. 2.1e). Ekman transport and Ekman pumping were significantly large during July, which might have been crucial causes of coastal upwelling

(Figs. 2.4b and 2.4c). However, both decreased dramatically as the wind speed decreased during August. It is obvious that the coastal upwelling in July was induced by the wind. However, a high UI persisted until the end of August despite the collapse of the upwelling-favourable wind. The slope of the interface increased during July and continued to have high values during August, as did the UI (Fig. 2.4d). This implies that the persistence of the coastal upwelling was closely related to the persistent dynamic uplift. The large sea level differences between the coastal and offshore regions continued after the plunge in the upwelling-favourable wind, as did the slope of the interface (Fig. 2.4e).

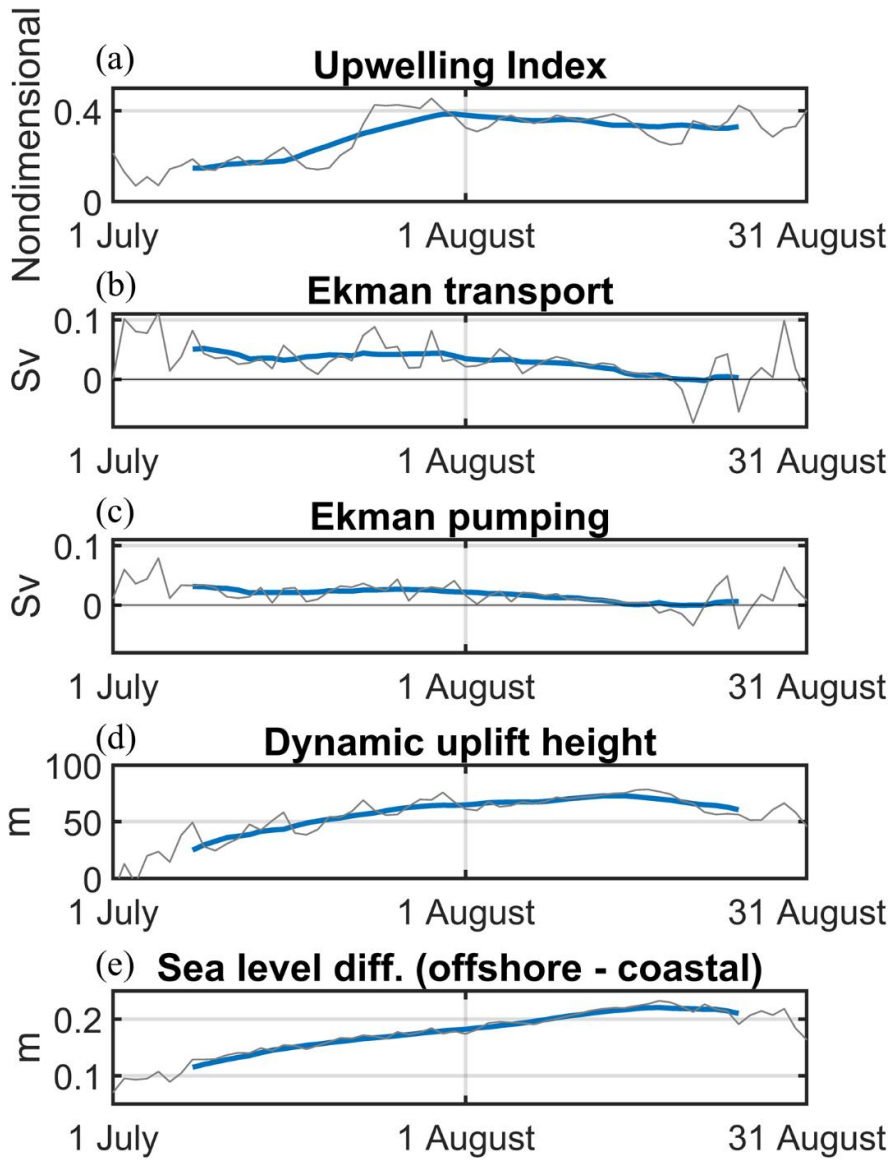

Figure 2.4 Time series of (a) the upwelling index, (b) Ekman transport, (c) Ekman pumping transport, (d) the slope of the interface, and (e) the sea level differences between the coastal and offshore regions from 1 July to 31 August, 2013. The grey and blue lines indicate the daily mean and the 2-week running mean, respectively.

2.3. Discussion and conclusions

It is known that most coastal upwelling events relax a few days after the upwelling-favourable winds weaken (Austin and Barth, 2002; Gan and Allen, 2002). However, coastal upwelling may continue, due to geostrophic equilibrium, for an extended period (Chen et al., 2017). The sea level decreases significantly in upwelling regions, which increases the cross-shore pressure gradient due to the sea level difference (Shi et al., 2000; Strub et al., 2015). The monthly mean sea level differences between July and August were determined from satellite data and from the model results (Fig. 2.5). The sea level differences in 2013 in the coastal region were much smaller than those determined using the 10 years mean data, whereas the sea level differences in the offshore region were almost the same. This suggests that the sea level in the coastal region during August 2013 was lower than that of the 10 years mean. The sea level in the upwelling area decreased during a period of upwelling-favourable winds from early July to late July. The decreased sea level was maintained after the weakening of the upwelling favourable wind in August. The decreased sea level in the upwelling region may have maintained the cross-shore pressure gradient in August.

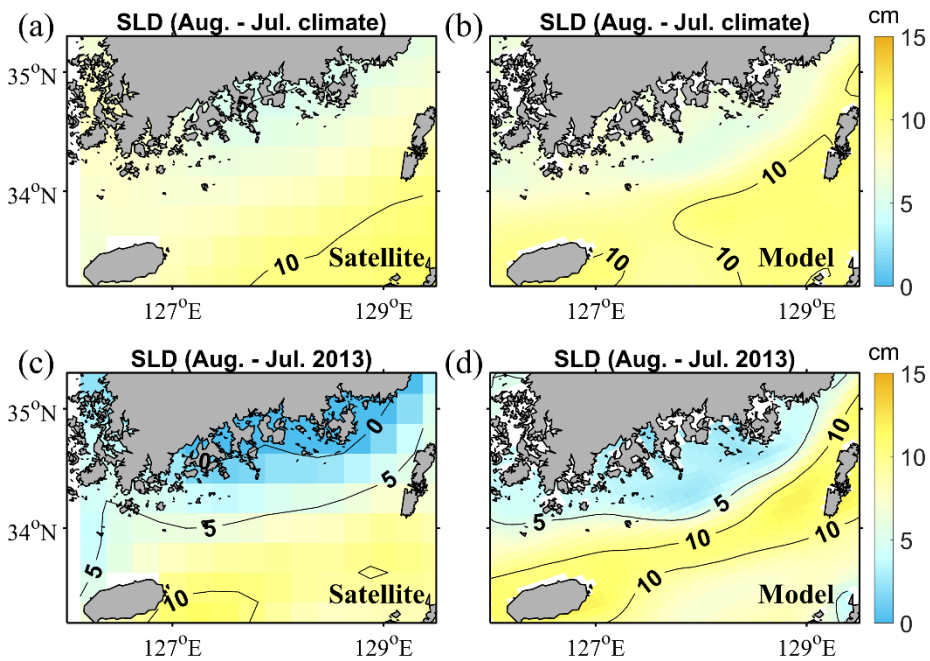

Figure 2.5 Sea level differences (SLD) between July and August as determined using the 10 years mean (2006–2015) from (a) satellite observations and (b) model results. Sea level differences between July and August 2013 from (c) satellite observations and (d) model results.

In the southern coastal region of the Korean Peninsula, the alongshore current flows eastward throughout the year (Pang et al., 2003; Teague et al., 2003). When wind-driven upwelling occurred in 2013, the intensified cross-shore pressure gradient strengthened the surface alongshore current. The increased surface velocity led to

a dynamic uplift due to the resulting geostrophic adjustment. The upwelled cold water that resulted from the dynamic uplift lowered the coastal steric sea level. The decreased sea level in the coastal area intensified the cross-shore barotropic pressure gradient, which induced a strong geostrophic current. However, the current in the lower layer decreased due to the baroclinic pressure gradient caused by the dynamic uplift. The intensified surface alongshore current subsequently produced a dynamic uplift due to the geostrophic adjustment.

Unprecedented coastal upwelling in the southern coastal region of the Korean Peninsula was reported via observational data measured during the summer of 2013. Observational data and model results obtained in this study show that the upwelling occurred due to upwelling-favourable wind during July. The upwelling persisted until the end of August, despite a weakening of the upwelling-favourable wind. After a plunge in the upwelling-favourable wind, a positive feedback between the dynamic uplift and geostrophic adjustment maintained the coastal upwelling for a month. The coastal upwelling that was driven by the upwelling-favourable wind lowered the sea level in the coastal region, which enhanced the surface alongshore current due to the cross-shore sea level difference. The

strong surface alongshore current maintained the dynamic uplift of deep, cold water in the coastal region due to the geostrophic equilibrium. Additional research is necessary to provide a dynamic explanation of the shut-down process of the upwelling in the study area.

2.4. Methods

2.4.1. Temperature observations

Two observational temperature datasets from 2006 to 2015 were used for this study. One was tidal station data that consisted of continuously observed data at 1 h intervals, which was obtained from the Korea Hydrographic and Oceanographic Agency (https://www.khoa.go.kr/oceangrid/koofs/kor/observation/obs_real.do). The other dataset was serial oceanographic observations obtained from the National Institute of Fisheries Science (https://www.nifs.go.kr/kodc/index.kodc). The serial oceanographic data have been routinely observed on a bimonthly basis at standard ocean depths around the Korean Peninsula.

2.4.2. Absolute dynamic topography

Satellite derived absolute dynamic topography (ADT) from 2006-2015 were obtained from the Copernicus Marine Environment Monitoring Service (CMEMS, https://marine.copernicus.eu/services-portfolio/access-to-products/?option=com_csw&view=details&product_id=SEALEVEL_GLO_PHY_L4_REP_OBSERVATIONS_008_047).

2.4.3. ROMS model setup

The numerical model used in this study was the Regional Ocean Modeling System (ROMS) (Shchepetkin and McWilliams, 2005), which is a free-surface, split-explicit, and hydrostatic ocean model that is characterised by a terrain-following curvilinear system. The model domain included the Yellow Sea, the East/Japan Sea, and part of the East China Sea (Fig. A4). The model grid had a resolution of 6-8 km horizontally and 40 vertical layers. ETOPO1 (Amante, 2009) (https://doi.org/10.7289/V5C8276M) and KorBathy30s (Seo, 2008) data were used for the bottom topography, with a minimum depth of 7 m. The initial temperature and salinity data were obtained from the

World Ocean Atlas 2018 (WOA 2018) (Locarnini et al., 2019; Zweng et al., 2019). HYCOM GOFS 3.0 reanalysis and analysis data were adopted for the open boundary (https://www.hycom.org/dataserver/gofs-3pt0). The 6 hourly data from the European Centre for Medium-Range Weather Forecasts (ECMWF) ERA5 reanalysis were used for the surface forcing, including temperature, wind, air pressure, and relative humidity (C3S, 2017). Daily mean values were used for solar radiation and precipitation. A bulk-flux formulation was used for calculating the surface flux (Fairall et al., 1996). Tidal forcing was applied along the open boundaries using ten major tidal components to include the tidal mixing effect that results from tidal elevation and tidal currents (Egbert and Erofeeva, 2002) (https://volkov.oce.orst.edu/tides/TPXO7.2.html). Discharges from 12 rivers were also included. Monthly mean river discharges at the Datong gauging station were used for the Changjiang River (https://www.cjh.com.cn/sqindex.html). River discharges for the other 11 rivers were obtained from the Global River Discharge Database (Vorosmarty et al., 1998) (https://doi.org/10.3334/ORNLDAAC/199). Vertical mixing was calculated using the K-profile parameterization mixing scheme (Large et al., 1994). Chapman, Flather, and clamped boundary conditions were used for the free-

surface, barotropic, and baroclinic momentums, respectively (Marchesiello et al., 2001). The horizontal viscosity coefficient was set to 100 m^2/s. The model was integrated for 15 years (from 2001 to 2015) after a 10 years spin-up run. The model results from 2006 onward were analysed.

2.4.4. ROMS momentum balance analysis

The momentum balance terms were calculated from the model results following Eqs. (2.1) and (2.2) by neglecting the acceleration, advection, diffusion, and horizontal viscosity terms (Fig. 2.3)

$$\underbrace{\frac{\partial u}{\partial t}}_{Acceleration} = - \underbrace{\frac{1}{\rho}\frac{\partial P}{\partial x}}_{Pressure\ gradient} + \underbrace{fv}_{Coriolis} + \underbrace{\frac{\partial}{\partial z}\left(A_z \frac{\partial u}{\partial z}\right)}_{Vertical\ viscosity}, \quad (2.1)$$

$$\underbrace{\frac{\partial v}{\partial t}}_{Acceleration} = - \underbrace{\frac{1}{\rho}\frac{\partial P}{\partial y}}_{Pressure\ gradient} - \underbrace{fu}_{Coriolis} + \underbrace{\frac{\partial}{\partial z}\left(A_z \frac{\partial v}{\partial z}\right)}_{Vertical\ viscosity}, \quad (2.2)$$

where u and v are the alongshore and the cross-shore velocity components, respectively, P is the pressure, ρ is the density of seawater, f is the Coriolis parameter, and A_z is the vertical eddy viscosity.

2.4.5. Upwelling index (UI) calculation

The UI was calculated using Eq. (2.3), which is a modified form of the UI suggested by Demarcq and Faure (Demarcq and Faure, 2000) based on the SST (Fig. 2.4a)

$$\mathrm{UI} = \frac{Temp_{offshore\,surface} - Temp_{coastal\,surface}}{Temp_{offshore\,surface} - Temp_{coastal\,bottom}}, \quad (2.3)$$

The modelled daily temperatures were used for the calculation. The surface temperature 150 km from the coast was chosen as the offshore temperature in each grid. UIs of 0 and 1 indicate no upwelling and the maximum upwelling, respectively. The UI was averaged along the coastal grids for each day.

2.4.6. Wind-driven upwelling transport

The wind-driven upwelling transport includes Ekman transport and Ekman pumping (Pickett and Paduan, 2003) (Figs. 2.4b and 2.4c). The Ekman transport in each coastal grid, M (m^3/s per meter of coast), was calculated after Smith (1968), as expressed by Eq. (2.4):

$$M = \frac{\vec{\tau}\cdot\hat{t}}{\rho f}, \quad (2.4)$$

where $\vec{\tau}$ is the wind-stress vector, $\hat{t}$ is a unit vector tangent to the coastline, ρ is the density of seawater, and f is a Coriolis parameter. The 6 h wind data were used to calculate the wind-driven upwelling.

Ekman transport was integrated along the coastal grid.

The Ekman pumping velocity, w (m/s), was calculated after Smith (Smith 1968) as defined in Eq. (2.5):

$$w = \hat{k} \cdot \nabla \times \frac{\vec{\tau}}{\rho f}, \quad (2.5)$$

where $\hat{k}$ is a unit vector in the local vertical direction. Ekman pumping velocities were integrated 100 km offshore from the coastal grid to calculate the Ekman pumping transport.

2.4.7. Slope of the interface

Assuming the geostrophic balance of two layers, the slope of the interface, $\partial h_2/\partial y$ (m/km), can be calculated from the daily mean of the model results (Fig. 2.4d) using Eq. (2.6):

$$\frac{\partial h_2}{\partial y} = \frac{f(u_1\rho_1 - u_2\rho_2)}{g(\rho_2 - \rho_1)}, \quad (2.6)$$

where ρ_1 is the density of the upper layer, ρ_2 is the density of the lower layer, u_1 is the alongshore velocity in the upper layer, and u_2 is the alongshore velocity in the lower layer. The selected density for the interface between the two layers was 1,024 kg/m3. The slope of the interface was averaged along the coast after the calculations using the model cross-shore vertical sections from the coastal grid to the grid 100 km offshore.

2.4.8. Sea level differences between the coastal and offshore regions

The sea level differences between the coastal and offshore regions were calculated from the daily mean model results (Fig. 2.4e). The sea level 100 km offshore was chosen as the offshore sea level. The sea level difference between the coastal and the offshore grids was spatially averaged along the coast.

3. Effects of surface heating on coastal upwelling intensity

3.1. Introduction

Upwelling in coastal regions is of particular interest to environmental researchers owing to its crucial role in coastal environmental studies. The process plays a key role in distributing not only heat and salt, but also nutrients and biological products in the upwelling region. Coastal upwelling can be induced for various reasons but generally results from Ekman transport due to alongshore winds (Ekman, 1905).

It is essential to quantitatively evaluate the coastal upwelling intensity, which can act as a proxy for estimating biological and chemical impacts on the coastal environment (Barth et al., 2007; Bode et al., 2009; García-Reyes et al., 2014; Pitcher et al., 2010; Tapia et al., 2009; Walter et al., 2014).

It is difficult to directly measure upwelling intensity because of the spatiotemporal variation in the upwelling response. Bakun (1973, 1975) constructed the Bakun index, which uses an alongshore component of wind stress to estimate the offshore Ekman transport. However, the Bakun index does not represent the change in ocean

state during a wind-driven upwelling.

For a supply of deep water to the surface, the isopycnal slope in the cross-shore direction has been utilized to estimate the coastal upwelling intensity (Austin and Barth, 2002). As the Ekman transport of coastal water is compensated by cold deep water, the isopycnal slope in the upwelling region tilts upward towards the coast and can be estimated by the vertical shear of alongshore currents (McCabe et al., 2015; Send and Nam, 2012).

Another widely utilized index for evaluating the coastal upwelling intensity is the difference in sea surface temperature (SST) between coastal and offshore regions (Benazzouz et al., 2014; Marcello et al., 2011; Nykjær and Van Camp, 1994). When coastal upwelling occurs, the decreased coastal SST increases the SST difference between coastal and offshore regions (Nykjær and Van Camp, 1994).

The effect of wind stress on upwelling intensity has been widely investigated (Chen et al., 2013; Enriquez and Friehe, 1995; Gill and Clarke, 1974; Wang, 1997). Surface offshore transport, which increases the upwelling intensity in coastal regions, largely depends on the alongshore surface wind stress (Smith, 1981).

A change in stratification can alter the upwelling source depth (He and Mahadevan, 2021; Jacox and Edwards, 2011) and surface

offshore velocity (Allen et al., 1995; Allen, 1973; Chen et al., 2019; Hsueh and Kenney III, 1972; Lentz and Chapman, 2004). Upwelling source depth has been shown to decrease as stratification intensifies (Jacox and Edwards, 2011; Lentz and Chapman, 2004). Intensified stratification in the water column confines the cross-shore circulation to a shallower near-surface layer (Hsueh and Kenney III, 1972). The change in the upwelling source depth and surface offshore velocity due to a change in stratification can affect the coastal upwelling intensity.

Changes in the upwelling intensity by increased surface heating, which frequently occur under global warming, are poorly understood. Previous studies have focused on the role of surface heating in warming the cold coastal SSTs related to coastal upwelling (Send et al., 1987; Spall and Schneider, 2016). Surface heating may warm the upwelled cold water and decrease the SST difference between the cold coastal and warm offshore regions.

However, a recent observational result demonstrated that the SST difference between the cold coastal and warm offshore regions increased during strong surface heating (Jung and Cho, 2020). A strong coastal upwelling along the southern coast of the Korean Peninsula was reported during the hot summer of 2013 (Fig. 3.1).

The air temperature and offshore SST in the summer of 2013 were higher than those of the climatological (2006-2015) mean by approximately 2 ° C. Despite the strong surface heating, the SST in the coastal upwelling region was lower than the climate SST by 2 ° C, resulting in a large temperature difference between the coastal and offshore regions.

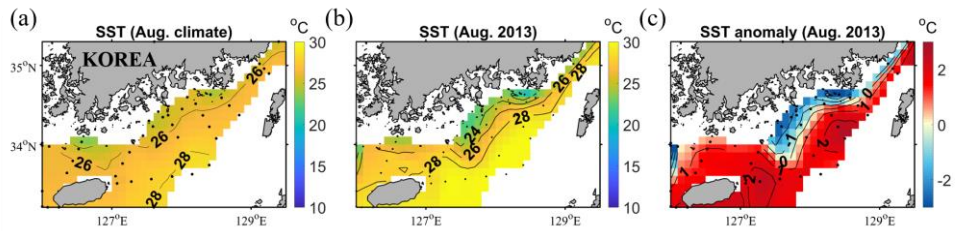

Figure 3.1 (a) Climate (2006–2015) SST in August, (b) SST in August 2013, and (c) SST anomaly in August 2013 in the southern coast of the Korean Peninsula. Black dots indicate the observation stations.

In the present study, simplified numerical experiments were conducted to explore the effect of surface heating on coastal upwelling intensity. The upwelling intensity was measured via an isopycnal slope and the SST difference between coastal and offshore regions. The change in upwelling intensity, at various wind speeds and surface heating levels, was investigated based on the upwelling

condition in the southern coast of the Korean peninsula (Jung and Cho, 2020).

This study does not consider other potential causes of upwelling, focusing on the effect of surface heating on the wind-driven upwelling intensity.

This chapter proceeds as follows: In section 3.2, the numerical model configuration is described. Section 3.3 describes upwelling responses according to various wind speeds and surface heating levels, including momentum and heat budgets. Section 3.4 is a discussion of the causes pertaining to the change in upwelling intensity. Section 3.5 provides a conclusion to this study.

3.2. Model setup

The numerical model utilized in this study is the Regional Ocean Modeling System (ROMS), which is a free-surface, split-explicit, and hydrostatic ocean model (Shchepetkin and McWilliams, 2005). The model domain is 500 km in length and 200 km in width (Fig. 3.2a) with a grid resolution of 1 km horizontally with 30 vertical layers. To capture the surface boundary structure precisely, fine vertical grid spacing (approximately 1 m) was implemented near the surface. The

bottom topography is flat with a uniform depth of 120 m to exclude the topographic effect. Vertical mixing was calculated using the MY-2.5 turbulent closure scheme (Mellor and Yamada, 1982). The background vertical eddy viscosity and diffusivity were set to $10^{-5}\,m^2s^{-1}$. The Coriolis parameter, $f = 10^{-4}\,s^{-1}$, was utilized, and the southern and northern boundaries were closed; the eastern and western boundaries were configured with periodic boundary conditions. The horizontal viscosity coefficient was set to $20\,m^2s^{-1}$, and the diffusivity coefficient was set to $2\,m^2s^{-1}$ (Ledwell et al., 1998). The initial temperature as a function of depth (Fig. 3.2b) was:

$$T(z) = 5 \times arctan\left(\frac{z+25}{15}\right) + 21, \qquad (3.1)$$

which represents a typical summer temperature profile on the southern coast of the Korean Peninsula. The salinity was set to a constant of 32 during the 25 numerical experiments, which were conducted with various wind speeds and surface heating values (Table 3.1). A bulk-flux formula was adapted to calculate the surface flux (Fairall et al., 1996, 2003). The wind stress, sensible heat, and latent heat were calculated using the Coupled Ocean-Atmosphere Response Experiment (COARE) 3.0 algorithm (Fairall et al., 2003). The bulk formulae for wind stress, sensible heat, and latent heat are given as follows:

$$\tau_x = \rho_a C_d S U, \quad (3.2)$$

$$Q_s = \rho_a c_P C_h S(SST - T_{air}), \quad (3.3)$$

$$Q_l = \rho_a L_e C_e S(q_{sea} - q_{air}), \quad (3.4)$$

where τ_x, Q_s, and Q_l are zonal wind stress, sensible heat flux, and latent heat flux, respectively; ρ_a is the density of air, C_d is the drag coefficient, S is the wind speed at a 10 m height, and U is the zonal wind speed at a 10 m height; c_P is the specific heat of air, C_h is the transfer coefficient for sensible heat, SST is the sea surface temperature, and T_{air} is the air temperature at a 2 m height; L_e is the latent heat of evaporation, $C_e$is the transfer coefficient for latent heat; and q_{sea} and q_{air} are the saturation specific humidity at the surface and at a 2 m height, respectively. The longwave radiation was calculated using the Berliand formula (Berliand, 1952) assuming zero cloud fraction.

The surface heating varied with air temperature and shortwave radiation. The air pressure and relative humidity for the bulk-flux formula were set to constants of 1007.5 hPa and 86.7%, respectively. The ranges of wind speed, air temperature, and shortwave radiation were based on the upwelling conditions on the southern coast of the Korean Peninsula during the summer (Jung and Cho, 2020). Shortwave radiation was imposed using a diurnal cycle. In each

experiment, spatially uniform air temperature, shortwave radiation, and upwelling-favorable (eastward) wind were applied after 10 days of adjustment for the initial conditions without any external forcing. The wind speed increased linearly to the assigned value for three days and was maintained for three days in each experiment.

The energy ranges of the wind speeds and surface heating imposed on the surface during the experiments were compared using the method reported by Simpson et al. (1978). The mean power ranges imposed by the wind stress and surface heating were comparable (Fig. 3.2c).

Zonally averaged model results were analyzed. The daily mean results of the experiments on the final day were considered. Altering the selected section did not substantially change the results.

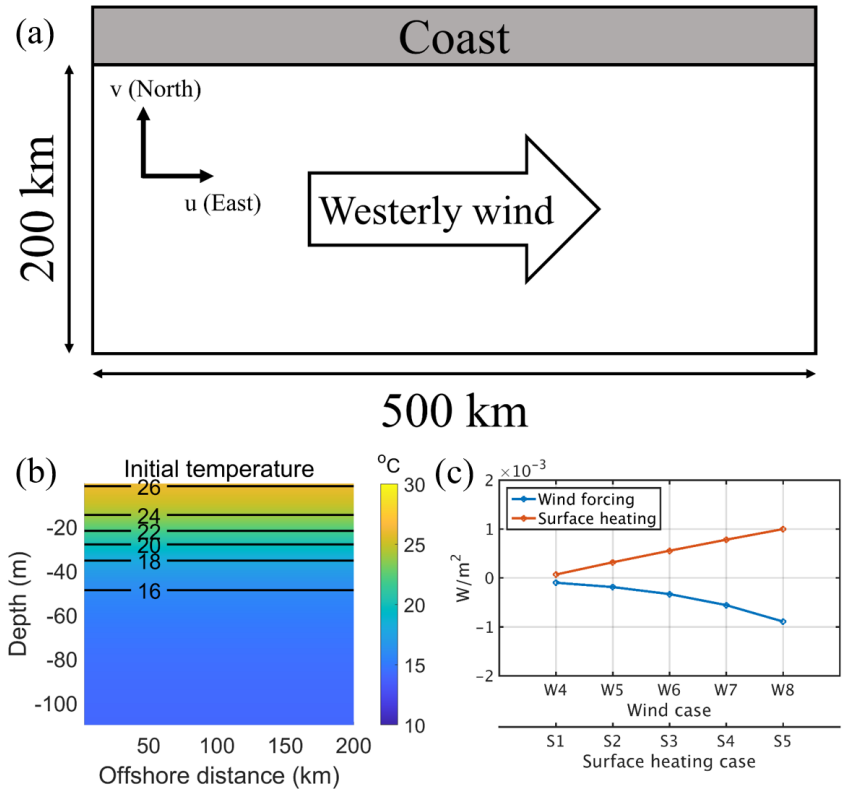

Figure 3.2 (a) A schematic of the model domain and wind direction. (b) Cross-shore section of initial temperature. (c) Comparison of the mean power imposed on the layer from the surface to 20 m by the surface wind stress and heating during the experiments. The red and blue lines represent the imposed power by surface heating and wind stress, respectively.

Table 3.1 Numerical experimental cases according to wind speed and surface heating. The surface heating varies according to the air temperature (AirT) and shortwave radiation (SWrad).

AirT & SWrad / Wind Speed	26 °C 100 W/m^2	27 °C 150 W/m^2	28 °C 200 W/m^2	29 °C 250 W/m^2	30 °C 300 W/m^2
4 m/s	W4_S1	W4_S2	W4_S3	W4_S4	W4_S5
5 m/s	W5_S1	W5_S2	W5_S3	W5_S4	W5_S5
6 m/s	W6_S1	W6_S2	W6_S3	W6_S4	W6_S5
7 m/s	W7_S1	W7_S2	W7_S3	W7_S4	W7_S5
8 m/s	W8_S1	W8_S2	W8_S3	W8_S4	W8_S5

3.3. Results

3.3.1. Vertical cross-sections of temperature and velocities

The vertical cross-sections of temperature, alongshore velocity, cross-shore velocity, and vertical velocity for cases employing weak (W4_S1 and W4_S5) and strong (W8_S1 and W8_S5) winds are

displayed in Figs. 3.3 and 3.4, respectively. The temperature sections exhibit coastal upwelling with the tilting of isopycnals (isotherms) toward the coast (Figs. 3.3a, 3.3e, 3.4a, and 3.4e). The isopycnal slope steepens as the wind speed increases and the surface heating decreases.

The SST of weak surface heating cases (Figs. 3.3a and 3.4a) is lower than that of strong surface heating cases (Figs. 3.3e and 3.4e) in both coastal and offshore regions. The surface-mixed layer becomes thicker with the increase in wind speed and decrease in surface heating. The temperature at a depth of 20 m exhibits insignificant change in all cases.

The alongshore velocities (Figs. 3.3b, 3.3f, 3.4b, and 3.4f) exhibit jet flow along the coast as a result of geostrophic adjustment by coastal upwelling. The maximum speed and thickness of the coastal jet are enhanced as the wind speed increases and the surface heating decreases. The cross-shore velocities (Figs. 3.3c, 3.3g, 3.4c, and 3.4g) display the offshore transport (negative value) driven by the alongshore wind near the surface. The surface boundary layer (SBL), where the offshore transport exists, becomes thicker as the wind speed increases and surface heating decreases. However, the maximum speed of the offshore velocity increases with an increase

in surface heating. The vertical velocities (Figs. 3.3d, 3.3h, 3.4d, and 3.4h) exhibit upward motion of subsurface water to compensate for the offshore transport. The vertical velocities increase as the wind speed increases. This results in an increased supply of subsurface water to the surface. The vertical velocity increases at a shallower depth but decreases at a deeper depth as the surface heating increases.

To clarify the changes in upwelling circulation, streamfunctions (ψ) combining cross-shore and vertical velocities are displayed in Fig. 3.5. The streamfunction is defined as $-\partial\psi/\partial z = v$ and $\partial\psi/\partial y = w$ where v is the cross-shore velocity and w is the vertical velocity. When the surface heating is strong (Fig. 3.5b and 3.5d), the streamlines near the surface become denser but the streamlines near the coast become sparser. This suggests that upwelling cells with strong surface heating are concentrated at shallower depths.

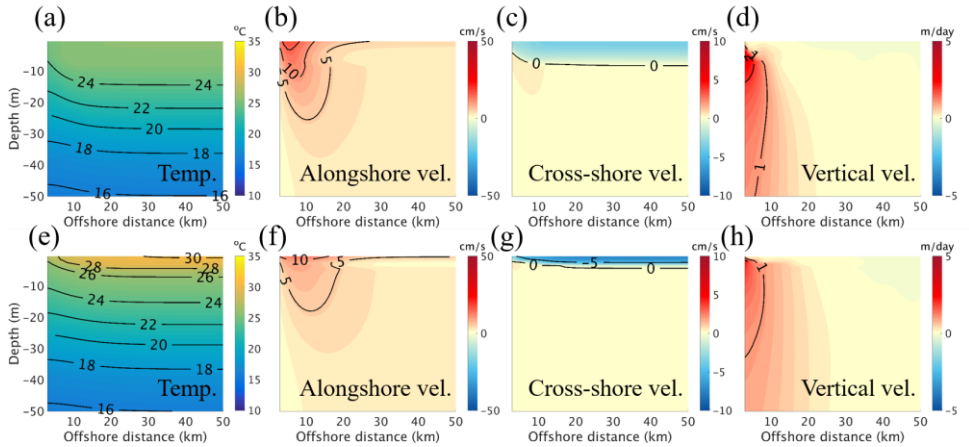

Figure 3.3 Cross-shore sections of temperature (Temp.), alongshore velocity (vel.), cross-shore velocity (vel.), and vertical velocity (vel.) on day 6 for W4_S1 (top) and W4_S5 (bottom). Positive values represent the eastward, northward (onshore), and upward directions in the alongshore, cross-shore, and vertical velocities, respectively.

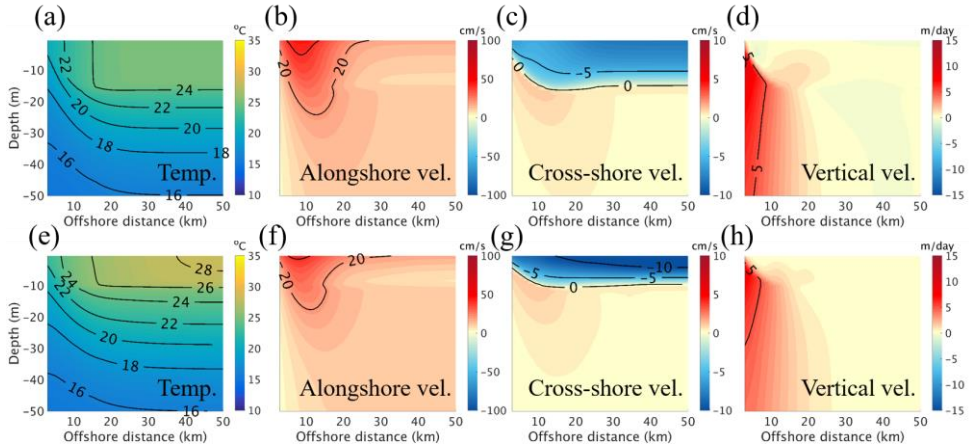

Figure 3.4 Cross-shore sections of temperature (Temp.), alongshore velocity (vel.), cross-shore velocity (vel.), and vertical velocity (vel.) on day 6 for W8_S1 (top) and W8_S5 (bottom). Positive values represent the eastward, northward (onshore), and upward directions in the alongshore, cross-shore, and vertical velocities, respectively.

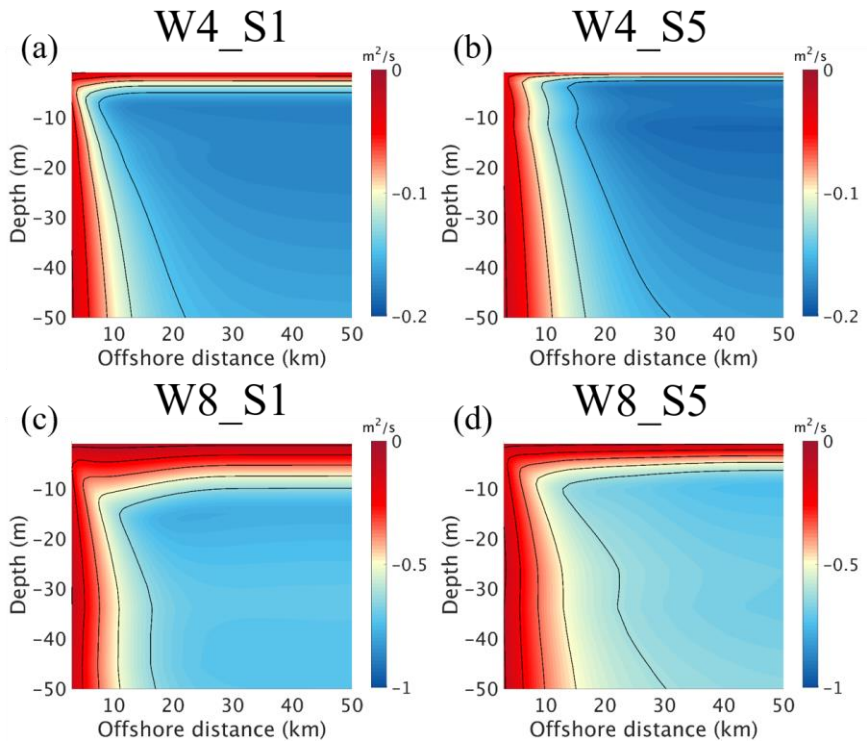

Figure 3.5 Calculated streamfunctions on day 6 for (a) W4_S1, (b) W4_S5, (c) W8_S1, and (d) W8_S5. The contour intervals are 0.1 m^2/s for W4 cases and 0.5 m^2/s for W8 cases.

3.3.2. Change in upwelling intensity according to wind speed and surface heating

Three upwelling indices were used to quantify the upwelling intensity in this study. The first upwelling index is offshore transport (V^s). The offshore transport was estimated as the transport above the shallowest zero crossing of the cross-shore velocity during three

windy days (Lentz and Chapman, 2004):

$$V^s = \int_{z_{v0}}^{0} v\, dz, \tag{3.5}$$

where v is the cross-shore velocity, and z_{v0} is the depth of the shallowest zero crossing of the cross-shore velocity.

The calculated offshore transport in each experimental case is displayed in Fig. 3.6a. The horizontal and vertical axes represent the variation in the maximum wind speed during each experiment and net surface heat flux (NSHF) on the first model day, respectively. The offshore transport does not change significantly according to the surface heating at the same wind speed, whereas it increases remarkably with the wind speed. The difference in the offshore transport is below 10% for cases with the same wind speed.

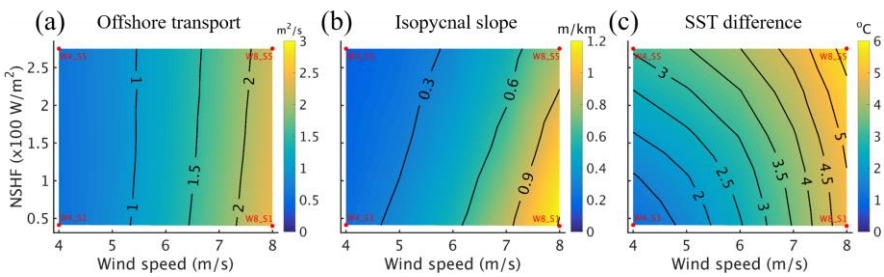

Figure 3.6 (a) Offshore transport, (b) isopycnal slope, and (c) sea surface temperature (SST) difference between the coastal and 50 km offshore regions on day 6 according to the wind speed and net surface heat flux (NSHF). Table 3.1 lists the wind speed and surface heating of each experimental case.

The second upwelling index is the isopycnal slope. The isopycnal slope was directly calculated assuming linearity using the 20 ° C isotherm line, which was not outcropped during the 6 days of the model run.

$$\left.\frac{\partial z}{\partial y}\right|_{T_{20}} = \frac{z_c - z_d}{d}, \tag{3.6}$$

where z_c is the depth of the 20 ° C isotherm line at the coast, and z_d is the depth of the 20 ° C isotherm line at d km from the coast. The value of d was set as 20 km for the isopycnal calculation because the depth of the 20 ° C isotherm line hardly changes at this distance during the model run.

The calculated isopycnal slope in each experimental case is displayed in Fig. 3.6b. The isopycnal slope increases as the wind speed increases, which corresponds to increased offshore transport. However, the slope decreases as the surface heating increases, as displayed in the thickness of the surface boundary layer (Figs. 3.3c, 3.3g, 3.4c, and 3.4g), which indicates that the change in isopycnal slope is caused by the changes in the thickness of the surface boundary layer.

The last upwelling index is an SST difference between coastal and offshore regions.

$$\Delta \mathrm{SST} = SST_o - SST_c, \tag{3.7}$$

where the SST_o and SST_c are the SST at the 50 km offshore and coastal regions, respectively.

The time series of SST in the coastal and offshore (50 km from the coast) regions for four cases (W4_S1, W4_S5, W8_S1, and W8_S5) are displayed in Fig. 3.7. When the surface heating is weak (S1), the offshore SSTs change slightly, while coastal SSTs decrease because of coastal upwelling. When the surface heating is strong (S5), the coastal SSTs decrease along with the weak surface heating cases, while the offshore SSTs increase because of the strong surface heating. Both coastal and offshore SSTs of the strong surface heating cases are higher than those of the weak surface heating cases. However, the increments of offshore SSTs are more pronounced compared with those of coastal SSTs, which means greater decreases in coastal SSTs because of active coastal upwelling under strong surface heating.

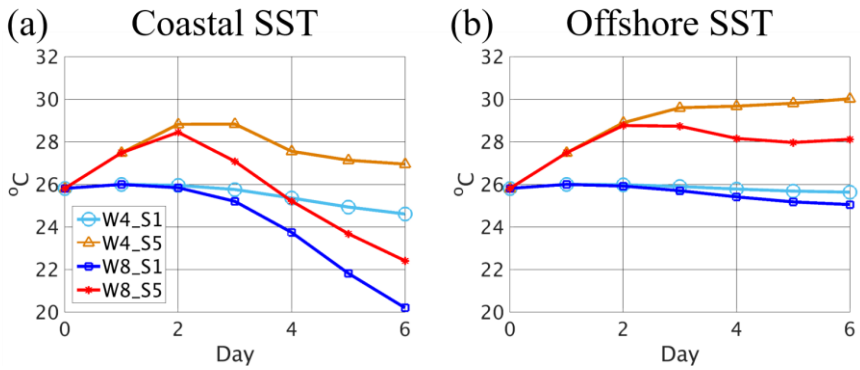

Figure 3.7 Time series of the sea surface temperature (SST) in the (a) coastal and (b) offshore (50 km from the coast) regions for four cases (W4_S1, W4_S5, W8_S1, and W8_S5). The horizontal axis represents the days after surface forcing is applied.

The SST differences between the coastal and offshore regions on the final day for varying wind speed and surface heating are displayed in Fig. 3.6c.

The SST difference increases as the wind speed increases, along with the isopycnal slope, which corresponds to the increased Ekman transport. Notably, the SST difference increases as the surface heating increases for all wind speeds.

To quantify the relationship of the surface heating to the change in upwelling intensity, the offshore transport, isopycnal slope, and SST difference were reconstructed using linear regression analysis based on the surface heating for each wind speed case as in Eq. (3.8):

$$\text{Upwelling index} = a \times \text{NSHF} + b, \tag{3.8}$$

where a is the slope of the line, and b is the intercept.

Before the linear regression analysis, the three upwelling indices were normalized by their maximum values. The results of linear regression are summarized in Table 3.2. As shown in Fig. 3.6, the offshore transport is relatively unaffected by the change in surface heating. Under stronger wind speed conditions, the decrease in isopycnal slope becomes more susceptible to the surface heating increase. In contrast, the increase in the SST difference is less sensitive to the surface heating under the stronger wind speed condition.

Table 3.2 Results of linear regression of upwelling intensity indices versus net surface heat flux (NSHF) as a function of wind speed with 95% confidence intervals.

Normalized upwelling index	Wind speed (m/s)	a $(/W \cdot m^{-2})$	b	Root mean square error (RMSE)
Offshore transport	4	$0.04 \pm 0.04\text{x}10^{-3}$	0.22 ± 0.01	0.0022
	5	$-0.03 \pm 0.08\text{x}10^{-3}$	0.35 ± 0.01	0.0044
	6	$-0.14 \pm 0.08\text{x}10^{-3}$	0.52 ± 0.01	0.0046
	7	$-0.25 \pm 0.07\text{x}10^{-3}$	0.74 ± 0.01	0.0039
	8	$-0.36 \pm 0.06\text{x}10^{-3}$	1.01 ± 0.01	0.0033
Isopycnal slope	4	$-0.26 \pm 0.07\text{x}10^{-3}$	0.18 ± 0.01	0.0041
	5	$-0.48 \pm 0.11\text{x}10^{-3}$	0.30 ± 0.02	0.0065
	6	$-0.78 \pm 0.14\text{x}10^{-3}$	0.48 ± 0.03	0.0084
	7	$-1.20 \pm 0.23\text{x}10^{-3}$	0.74 ± 0.04	0.0133
	8	$-1.49 \pm 0.31\text{x}10^{-3}$	1.08 ± 0.06	0.0179
SST difference	4	$1.54 \pm 0.21\text{x}10^{-3}$	0.10 ± 0.04	0.0120
	5	$1.40 \pm 0.29\text{x}10^{-3}$	0.21 ± 0.05	0.0165
	6	$1.16 \pm 0.34\text{x}10^{-3}$	0.36 ± 0.06	0.0195
	7	$0.87 \pm 0.30\text{x}10^{-3}$	0.57 ± 0.05	0.0176
	8	$0.63 \pm 0.25\text{x}10^{-3}$	0.81 ± 0.05	0.0146

3.3.3. Momentum balance

Alongshore and cross-shore momentum balances in the cross-shore section were calculated to understand the upwelling dynamics

that determine the upwelling intensity in response to the changes in wind speed and surface heating. The nonlinear advection term in the alongshore momentum balances is significant near the upwelling front region when the wind speed is strong. However, except that region, the advection term is small, on the order of $O(10^{-9})\ m/s^2$, while the other significant terms have orders of $O(10^{-6})\ m/s^2$. The momentum equations neglecting the small advection, diffusion, and horizontal viscous force terms can be expressed by Eqs. (3.9) and (3.10):

$$\frac{\partial u}{\partial t} = -\frac{1}{\rho}\frac{\partial P}{\partial x} + fv + \frac{\partial}{\partial z}\left(A_z \frac{\partial u}{\partial z}\right), \tag{3.9}$$

$$\frac{\partial v}{\partial t} = -\frac{1}{\rho}\frac{\partial P}{\partial y} - fu + \frac{\partial}{\partial z}\left(A_z \frac{\partial v}{\partial z}\right), \tag{3.10}$$

where u and v are the alongshore and cross-shore velocity components, respectively, ρ is the density of seawater, P is the pressure, f is the Coriolis parameter, and A_z is the vertical eddy viscosity. Because the acceleration terms are balanced by a combination of the pressure gradient force (PGF), Coriolis force, and vertical viscous force terms, only the right-hand side terms in Eqs. (3.9) and (3.10) are plotted. The alongshore and cross-shore momentum balances on the final day for the four cases (W4_S1, W4_S5, W8_S1, and W8_S5) are displayed in Figs. 3.8 and 3.9.

In the alongshore direction (Fig. 3.8), the PGF of each case has an order of $O(10^{-12})\ m/s^2$, which is small enough to be neglected.

However, the Coriolis and vertical viscous forces are balanced near the surface, which results in the development of the SBL. The SBL becomes thicker as the wind speed increases and thinner as the surface heating increases. However, the Coriolis and vertical viscous forces become stronger with the increase in surface heating, as shown in the offshore velocities (Figs. 3.3c, 3.3g, 3.4c, and 3.4g) and SST difference (Fig. 3.6c). This implies that the offshore velocities and SST difference are closely related to the thickness of the SBL.

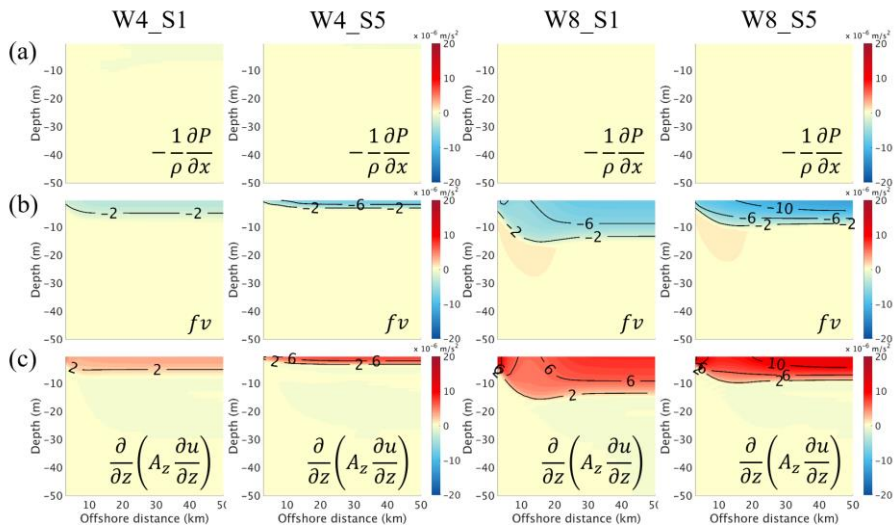

Figure 3.8 Alongshore momentum balance terms with the (a) pressure gradient force, (b) Coriolis force, and (c) vertical viscous force on day 6 for four cases (W4_S1, W4_S5, W8_S1, and W8_S5)

In the cross-shore direction (Fig. 3.9), a geostrophic coastal jet exists in which the PGF and Coriolis force were balanced during the

wind-driven upwelling. The PGF and Coriolis force in the coastal region become stronger as the wind speed increases and the surface heating decreases, as displayed in the alongshore velocities (Figs. 3.3b, 3.3f, 3.4b, and 3.4f) and isopycnal slope (Fig. 3.6b).

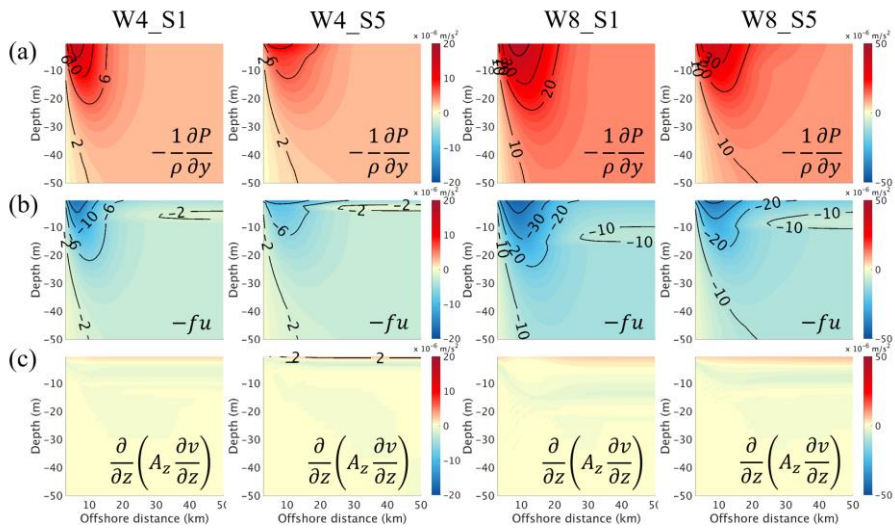

Figure 3.9 Cross-shore momentum balance terms with the (a) pressure gradient force, (b) Coriolis force, and (c) vertical viscous force on day 6 for four cases (W4_S1, W4_S5, W8_S1, and W8_S5). The contour intervals are $4 \times 10^{-6}\, m/s^2$ for W4 cases and $10 \times 10^{-6}\, m/s^2$ for W8 cases.

3.3.4. Heat balance in the surface layer

The heat balance in the surface layer was calculated to investigate the main causes of SST variations in the coastal and

offshore regions. The heat balance equation, neglecting the small alongshore advection and horizontal diffusion terms can be expressed by Eq. (3.11):

$$\frac{\partial T}{\partial t} = -\frac{\partial (vT)}{\partial y} - \frac{\partial (wT)}{\partial z} + \frac{\partial}{\partial z}\left(A_{kt}\frac{\partial T}{\partial z}\right). \quad (3.11)$$

The surface and bottom boundary conditions are as follows:

$$\left(A_{kt}\frac{\partial T}{\partial z}\right)_{z=0} = \frac{Q_{net}}{\rho_0 C_p} \quad (3.12)$$

$$\left(A_{kt}\frac{\partial T}{\partial z}\right)_{z=-h} = 0, \quad (3.13)$$

where T is the temperature, v is the cross-shore velocity, w is the vertical velocity, A_{kt} is the vertical diffusivity, Q_{net} is the net surface heat flux, $\rho_0 = 1025\, kg\, m^{-3}$ is the reference density, and $C_p = 3985\, J\, (kg℃)^{-1}$ is the specific heat capacity of seawater.

To evaluate the effect of surface heating on SST variations, the third term on the right-hand side of Eq. (3.11) was decomposed into downward vertical heat diffusion from the uppermost model layer to the second layer ($\mathrm{V\_DIFF_{down}}$) and the difference between net surface heat flux to the first layer and transmission of solar radiation to the second layer in the model ($\mathrm{V\_DIFF_{SHF}}$).

$\mathrm{V\_DIFF_{down}}$ was calculated using the following equation:

$$\mathrm{V\_DIFF_{down}} = \frac{1}{\partial z}\left(-A_{kt}\frac{\partial T}{\partial z}\right). \quad (3.14)$$

$\mathrm{V\_DIFF_{SHF}}$ was calculated using the following equation:

$$\mathrm{V\_DIFF_{SHF}} = \frac{1}{\partial z}\left(\frac{Q_{net}}{\rho_0 C_p} - \frac{Q_{s1}}{\rho_0 C_p}\right), \quad (3.15)$$

where Q_{s1} is the solar radiation penetrating the bottom of the first layer.

The cumulative time integrals of heat balance in the offshore and coastal regions on day 6 are displayed in Fig. 3.10.

The cross-shore advection (H_ADV) and vertical advection (V_ADV) terms were combined into the total advection term (Fig. 3.10) to evaluate the net effect of advection.

$$\mathrm{ADV} = \mathrm{H\_ADV} + \mathrm{V\_ADV} = -\frac{\partial(vT)}{\partial y} - \frac{\partial(wT)}{\partial z}. \quad (3.16)$$

The change in offshore SST (Fig. 3.7b) depends on the surface heat flux and downward vertical diffusion (Fig. 3.10b). When the surface heating is strong, the SST increases because of the surface heat flux but decreases because of the downward vertical diffusion. The effect of advection on the change in offshore SST (ADV in Fig. 3.10b) is negligible and can be ignored. There was no significant change in offshore SST in the weak surface heating cases (Fig. 3.7b) because of the balance between the surface heat flux and downward vertical diffusion.

The change in coastal SST (Fig. 3.7a) depends on not only the surface heat flux and the downward vertical diffusion but also

advection (Fig. 3.10a). Except for case W4_S1, SST increased owing to the surface heat flux and decreased owing to the downward vertical diffusion). For W4_S1, the surface heating was not strong enough to increase the SST. When the surface heating is strong, an increase in SST caused by the surface heat flux is more pronounced compared with that in weak surface heating cases. The impact of advection on SST change becomes significant in the coastal region (ADV in Fig. 3.10a). A decrease in SST caused by advection is more obvious when the surface heating is strong.

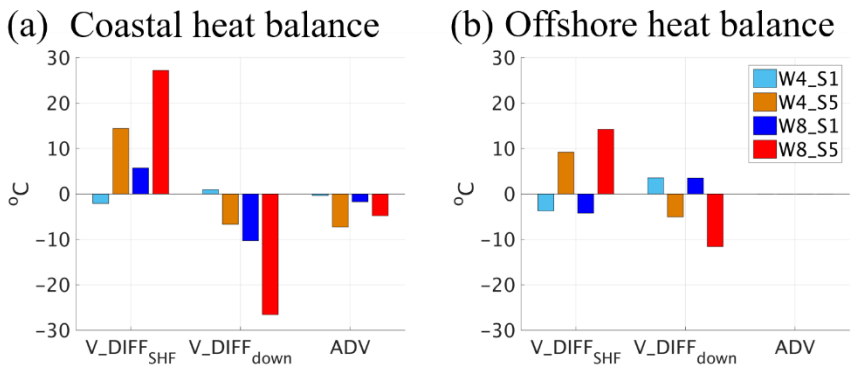

Figure 3.10 Cumulative time integrals of heat balance in the (a) coastal and (b) offshore regions on day 6 for four cases (W4_S1, W4_S5, W8_S1, and W8_S5). The horizontal axis represents the heat balance terms in Eqs. (3.14)–(3.16).

3.4. Discussion

3.4.1. Effect of surface heating on total upwelling transport and surface boundary layer thickness

The offshore transport calculated by model velocities (Fig. 3.6a) was compared with total upwelling transport, which is the sum of Ekman transport (V^{EK}) and Ekman pumping transport. The Ekman transport, which was calculated as described by Smith (1968), is defined in Eq. (3.17):

$$V^{EK} = \frac{\tau^x_{coast}}{\rho_0 f}, \tag{3.17}$$

where τ^x_{coast} is the alongshore wind−stress in the coastal region.

The Ekman pumping velocity, $w_E\,(m/s)$, which was also calculated as described by Smith (1968), is defined in Eq. (3.18):

$$w_E = \frac{1}{\rho_0 f}\left(-\frac{\partial \tau^x}{\partial y}\right), \tag{3.18}$$

where τ^x is the alongshore surface wind stress.

The wind stress from the numerical model output was used for the calculations. The Ekman pumping velocities were integrated from the coastal grid to the 50 km offshore grid for the Ekman pumping transport. The calculated results are displayed in Fig. 3.11. The total

upwelling transport (Fig. 3.11a) is comparable to the offshore transport in Fig. 3.6a ($R^2 = 0.9995$ and RMSE $= 0.0153$). Although the total upwelling transport exhibits little change as the surface heating increases, the Ekman transport decreases (Fig. 3.11b) but the Ekman pumping transport increases (Fig. 3.11c). Thus, the surface heating can change the Ekman transport and Ekman pumping transport at the same wind speed.

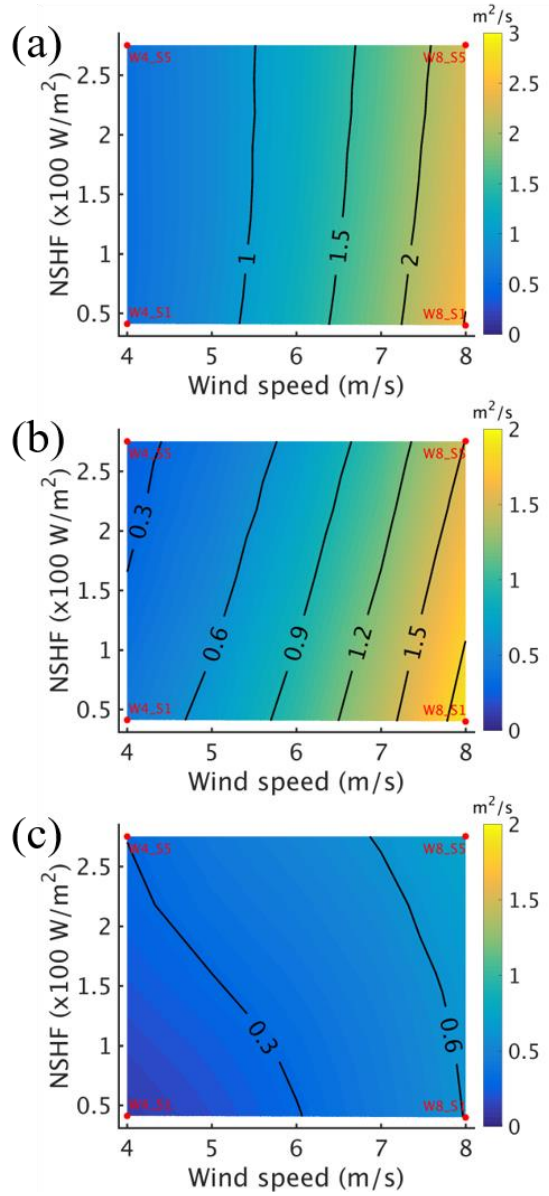

Figure 3.11 (a) Total upwelling transport, (b) Ekman transport, and (c) Ekman pumping transport on day 6 according to the wind speed and NSHF. Table 3.1 lists the wind speed and surface heating for each experimental case.

In the ROMS model, surface wind stress is calculated using the

bulk-flux formula. As seen in Eq. (3.2), the surface wind stress changes with the drag coefficient (C_d), which depends on the air-sea stability conditions (Fairall et al., 2003). COARE3.0 C_d was parameterized as a function of air-sea stability, gustiness, and surface roughness as in Eq. (3.19), based on the Monin-Obukhov similarity theory.

$$C_d{}^{1/2}(\zeta) = \frac{C_{dn}{}^{1/2}}{\left[1-\frac{C_{dn}{}^{1/2}}{\kappa}\psi_d(\zeta)\right]}, \qquad (3.19)$$

where ζ is a stability parameter, the subscript n refers to neutral stability, κ is von Karman's constant, and ψ_d is an empirical function describing the stability dependence of the mean profile. The C_d calculated from the COARE algorithm can be expressed as a function of air-sea temperature difference (Kara et al., 2005). Assuming constant air pressure (1007.5 hPa) and relative humidity (86.7%), the C_d for various wind speeds is displayed in Fig. 3.12 as a function of air-sea temperature difference. As the stability increases due to decreasing SST by upwelling, the C_D decreases, which results in weak wind stress. Colder coastal water caused by coastal upwelling decreases the wind stress in coastal regions, which weakens Ekman transport. However, the increased stability by the cold surface water induces the wind stress curl and enhances Ekman pumping. Strong surface heating, which results in a larger SST

difference between coastal and offshore regions, increases Ekman pumping. The increase in Ekman pumping and decrease in Ekman transport due to the air–sea stability are consistent with the findings of previous studies that used an empirical SST–wind interaction relationship (Chelton et al., 2007; Jin et al., 2009). This stability–induced wind stress curl can significantly affect the upwelling source depth (Jacox and Edwards, 2012) and the subsurface density structure (Capet et al., 2004).

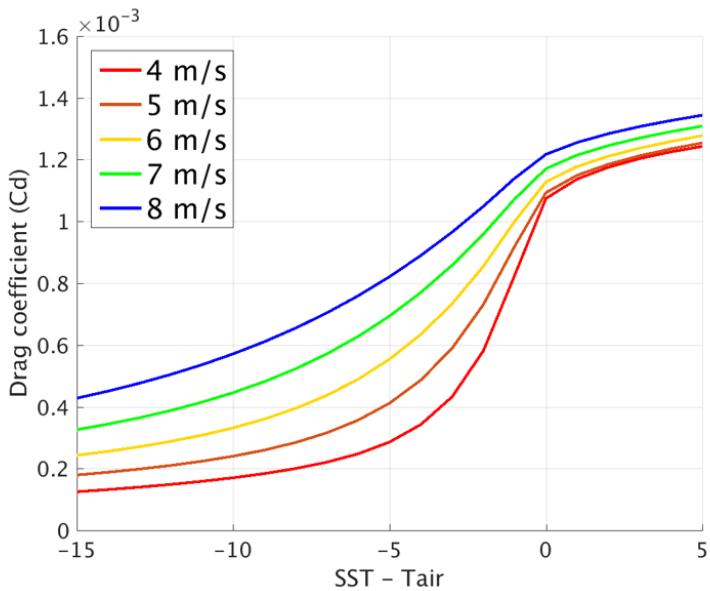

Figure 3.12 Drag coefficients for various wind speeds. The horizontal axis represents the difference between SST and air temperature (Tair). Color indicates the wind speed as shown in the legend.

As shown in Figs. 3.3, 3.4, and 3.8, the thickness of the SBL (H_{SBL})

decreases but the maximum speed of the offshore velocity increases with surface heating. The scale of H_{SBL} is $\sqrt{2A_z/f}$, where A_z is the vertical eddy viscosity (Ekman, 1905; Price and Sundermeyer, 1999). Thus, the H_{SBL} and vertical eddy viscosity display a proportional relationship. The offshore velocity in the SBL is closely related to the vertical eddy viscosity (Austin and Lentz, 2002; Lentz, 1995). Austin and Lentz (2002) reported an inverse dependence of vertical eddy viscosity on water column stratification. The vertical eddy viscosity is considered proportional to the mixing length in the surface-mixed layer, which is bounded by the air-sea interface (Munk and Anderson, 1948). Below the surface-mixed layer, the vertical eddy viscosity decreases with an increase in Richardson number (Ri) (Forryan et al., 2013; Simpson et al., 2005).

The cross-shore sections of the vertical eddy viscosity for four cases (W4_S1, W4_S5, W8_S1, and W8_S5) are displayed in Fig. 3.13. The vertical eddy viscosities have an order of O $(10^{-5} - 10^{-3})\, m^2/s$, which are typical values of other upwelling regions (Djurfeldt, 1989; Xie et al., 2017).

The vertical eddy viscosity is prominent from the surface to the depth at which the Coriolis and vertical viscous forces are in balance (Fig. 3.8). The threshold depths of the prominent vertical viscous

force are consistent with the depth of Ri = 1 (lower red dashed lines in Fig. 3.13). The vertical eddy viscosity increases as the wind speed increases and the surface heating decreases. When the surface heating is weak (Figs. 3.13a and 3.13c), the mixed layer depth (MLD) is relatively thick, and vertical surface mixing is enhanced. The enhanced vertical mixing results in an increase in the vertical eddy viscosity because of an increase in the mixing length (Munk and Anderson, 1948) and a decrease in Ri (Forryan et al., 2013; Simpson et al., 2005). The increased vertical eddy viscosity increases the SBL thickness but decreases the offshore velocity, while the offshore transport remains unchanged.

In contrast, when the surface heating is strong (Fig. 3.13b and 3.13d), the MLD becomes thinner and vertical mixing is inhibited. The inhibited vertical mixing results in a decrease in the vertical eddy viscosity because of the decreased mixing length and increased Ri in the SBL. Owing to the decreased vertical eddy viscosity, the surface stress is limited to the shallow surface, which results in a thin SBL but enhanced offshore velocity.

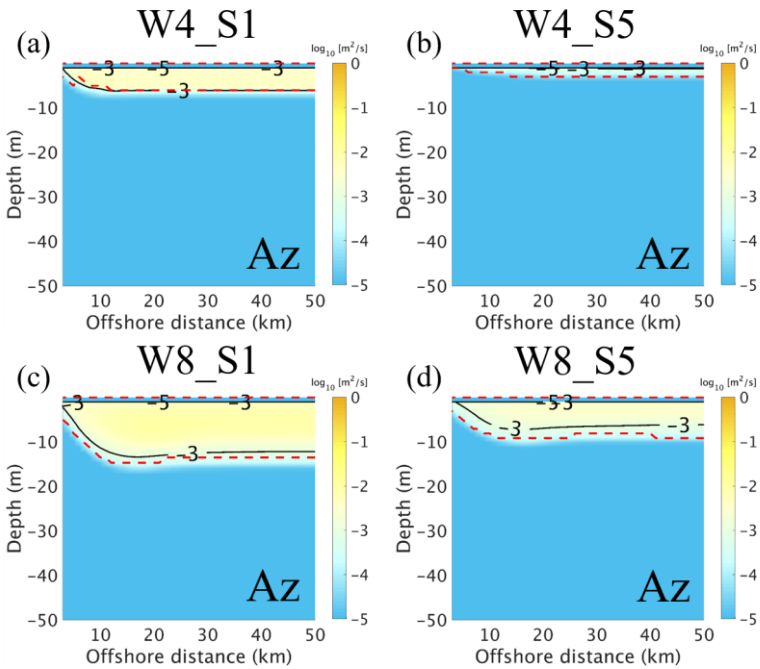

Figure 3.13 Cross-shore sections of the vertical eddy viscosity (Az) on day 6 for (a) W4_S1, (b) W4_S5, (c) W8_S1, and (d) W8_S5. The upper and lower red dashed lines represent the air-sea interface and depth of Ri = 1, respectively.

Vertical profiles of the offshore velocities calculated by a simple analytical model for the Ekman layer (Wenegrat and McPhaden, 2016) were compared with model results (Fig. 3.14). Wind stress and vertical eddy viscosity calculated from the numerical model were used as input parameters for the analytical model. Depth-averaged vertical eddy viscosity was used for surface (z=0) vertical eddy viscosity in this study. δ and f/ω were set to 0.75 and 0.9, respectively (Wenegrat and McPhaden, 2016). Although there are

differences in absolute values, the changes in the speed and thickness of the SBL caused by the surface heating are comparable in both models. The differences may be attributable to the space–time coupling of vertical eddy viscosity calculated from the numerical model.

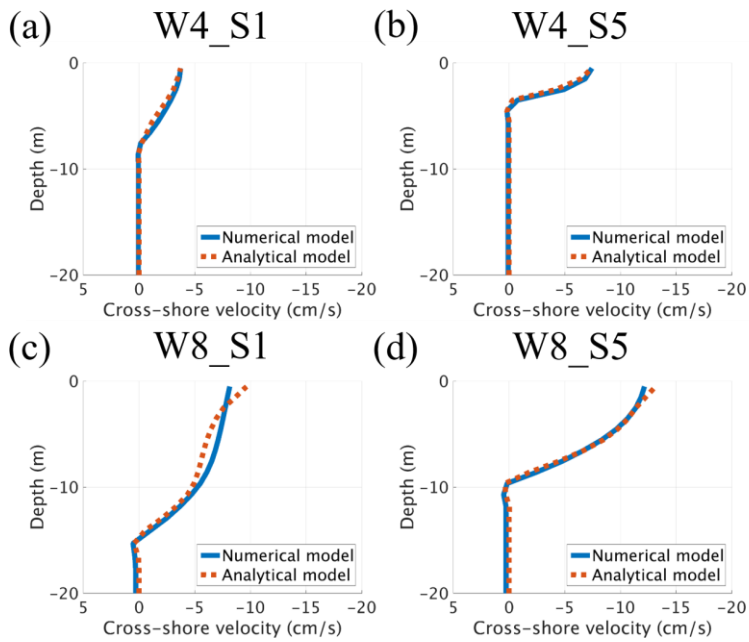

Figure 3.14 Vertical profiles of the offshore velocities (50 km from the coast) on day 6 for (a) W4_S1, (b) W4_S5, (c) W8_S1, and (d) W8_S5. Blue lines represent cross–shore velocities from the numerical model and orange dotted lines represent the cross–shore velocities calculated from the analytical model.

3.4.2. Change in isopycnal slope according to the surface boundary layer thickness

The isopycnal slope may result from the vertical and horizontal scales of upwelling motion (Lentz and Chapman, 2004). The isopycnal slope should be proportional to the water depth divided by the baroclinic Rossby radius of deformation (L_d) (Lentz and Chapman, 2004). The H_{SBL}, which determines the depth from which fluid is drawn into the SBL, was selected as the vertical scale of upwelling motion in this study because it is closely related to the isopycnal slope. L_d is a horizontal scale for sloping isopycnals during upwelling (Allen, 1980; Pedlosky, 1978). The L_d for the two-layer fluid is defined as:

$$L_d = \sqrt{\frac{g'\left(\frac{H_1 H_2}{H_1+H_2}\right)}{f^2}}, \qquad (3.20)$$

where g' is the reduced gravity, f is the Coriolis parameter, and H_1 and H_2 are the thicknesses of the upper and lower layers, respectively (Gill and Clarke, 1974).

To calculate the L_d, H_1 was chosen as H_{SBL} at 50 km offshore where the subsurface density changes little during the experiments; g' was calculated utilizing the mean densities of H_1 and H_2. H_{SBL} is

defined as the depth of Ri = 1. Ri is defined as:

$$Ri = \frac{N^2}{\left(\frac{\partial u}{\partial z}\right)^2 + \left(\frac{\partial v}{\partial z}\right)^2}, \tag{3.21}$$

where N is the buoyancy frequency, u is the alongshore velocity, and v is the cross−shore velocity.

The ratio of H_{SBL} to L_d, assuming $H_1 \ll H_2$, can be expressed as:

$$\sqrt{\frac{H_1}{g'}} f. \tag{3.22}$$

H_{SBL} and L_d were calculated for each experiment (W4_S1, W4_S5, W8_S1, and W8_S5) as displayed in Table 3.3. The change in L_d due to surface heating is noticeably smaller than that of H_{SBL}. This is due to the effect of increasing g' being offset by decreasing $H_1 (= H_{SBL})$ in Eq. (3.20). The smaller variation in L_d relative to that in H_{SBL} suggests that H_{SBL} is crucial in determining the isopycnal slope during surface heating. This results in a gentle isopycnal slope with the increase in surface heating because surface heating forms a thinner SBL.

Table 3.3 Thickness of the surface boundary layer (H_{SBL}) and baroclinic Rossby radius of deformation (L_d) for four cases (W4_S1, W4_S5, W8_S1, and W8_S5).

Case	H_{SBL} (m)	L_d (km)	H_{SBL}/L_d (m/km)
W4_S1	6.03	2.64	2.28
W4_S5	3.00	2.60	1.15
W8_S1	13.78	4.25	3.24
W8_S5	8.60	4.00	2.15

The ratio of H_{SBL} to L_d was plotted with the model-calculated isopycnal slope (Fig. 3.15). The isopycnal slope and ratio of H_{SBL} to L_d show a proportional linear relationship consistent with the results of Lentz and Chapman (2004). The proportionality constants with 95% confidence intervals for wind speeds of 4, 5, 6, 7, and 8 m/s are 0.06 ± 0.01, 0.11 ± 0.01, 0.18 ± 0.01, 0.29 ± 0.02, and 0.38 ± 0.08, respectively. The increasing proportionality constant with increasing wind speed suggests that the dependence of the isopycnal slope on the ratio of H_{SBL} to L_d becomes stronger as the wind speed increases.

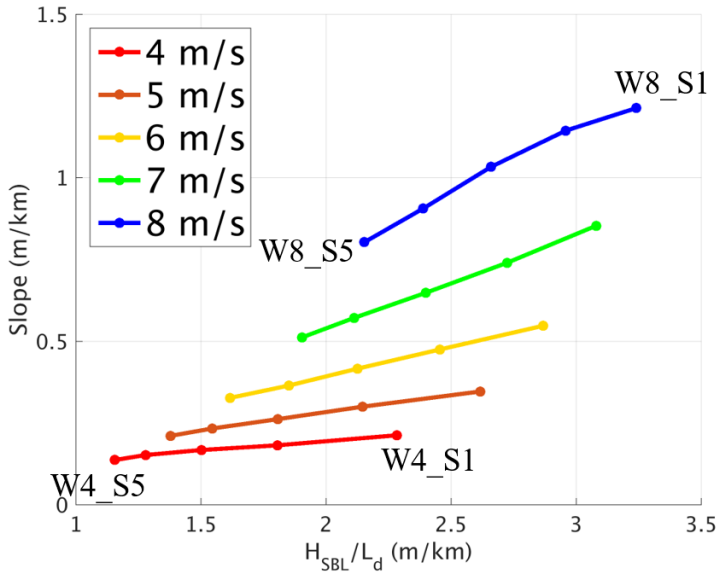

Figure 3.15 Isopycnal slope as a function of the ratio of thickness of surface boundary layer (H_{SBL}) to Rossby radius of deformation (L_d) on day 6. Color indicates the wind speed as shown in the legend.

3.4.3. Two opposing effects of surface heating on SST difference between coastal and offshore regions

Surface heating warms the cold SSTs in the upwelling region and it is expected that surface heating may decrease the SST difference between the coastal and offshore regions. However, the model exhibited the opposite result, with the SST difference between the coastal and offshore regions increasing as the surface heating increases (Fig. 3.9). The difference in the heat balance between the

coastal and offshore regions was calculated to determine the causes of the change in the SST difference. The difference in the heat balance between coastal and offshore regions is presented as a cumulative time integral (Fig. 3.16). V_DIFF_{SHF} and V_DIFF_{down} were combined into a single vertical diffusion term (Fig. 3.16a).

Vertical diffusion (Fig. 3.16a) contributes less to the SST difference (Fig. 3.16c) in the cases of strong surface heating than in the cases of weak surface heating owing to increasing V_DIFF_{SHF} in the coastal region (Fig. 3.10a). This implies that the SST difference between the coastal and offshore regions decreases because of increased net surface heat flux. However, the SST difference increases consequently (Fig. 3.16c) because of advection (Fig. 3.16b).

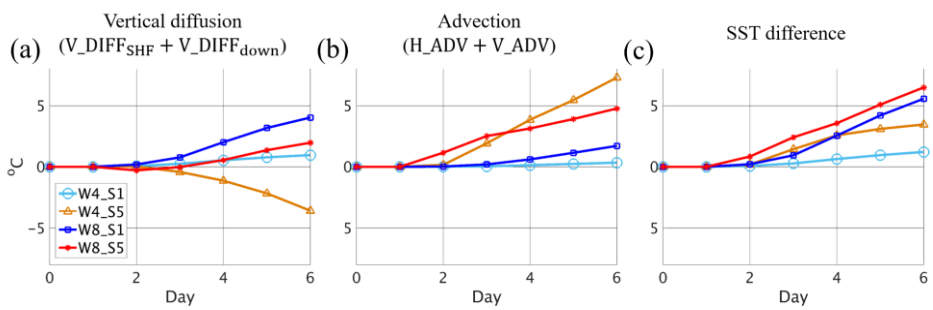

Figure 3.16 Time series of the differences in the heat balance between coastal and offshore regions presented as a cumulative time integral. (a) Changes in sea surface temperature (SST) difference from vertical diffusion. (b) Changes in SST difference from advection. (c) Changes in SST difference. The horizontal axis represents the days after surface forcing is applied.

3.4.4. Limitations and implications

Model results from the simplified model, assuming a flat bottom and no alongshore variability, may differ from the realistic responses in the coastal region. Steep bottom topography leads to narrow and intense upwelling circulation, whereas gentle bottom topography results in broad and weak upwelling circulation (Allen et al., 1995; Chen et al., 2013; Estrade et al., 2008). Thus, the model results with a flat bottom may weaken the cross-shore return flow because the bottom Ekman transport cannot be considered, potentially weakening the effect of surface heating compared with the realistic response in the coastal region. The presence of the alongshore pressure gradient can also affect the near surface cross-shore transport (Jacox et al., 2018; Marchesiello and Estrade, 2010) and surface temperature in the true coastal region (Gan and Allen, 2002; Send et al., 1987). Therefore, the findings in this study may not be applicable when the effect of alongshore pressure gradient is significant.

The numerical model results are transient states in this study. In a stratified ocean, cross-shore circulation induced by upwelling-favorable wind is unsteady and exhibits offshore movement for the sloping isopycnals and upwelling front (Allen et al., 1995; Lentz and

Chapman, 2004). The unsteady response of numerical models precludes the quantitative generalization of model results. However, when the model was run longer, no changes in the relative effect of surface heating on the offshore transport, isopycnal slope, and SST were observed. The main factors controlling the offshore transport and isopycnal slope are the offshore wind stress and SBL thickness. The relative effect of these factors continues for a longer time. Although the lower temperature waters in the upwelled region absorb heat faster than warmer offshore waters over time, the faster offshore velocity continuously maintains a larger cross-shore temperature difference.

In spite of these limitations, the findings presented in this study can help us understand the role of surface heating in changing the upwelling system for the future climate scenarios. Strong surface heating enhances the surface offshore velocity, which suggests that the surface coastal water can move farther offshore while the upwelling source depth decreases. This change can significantly affect the circulation and ecosystem in the coastal upwelling region (Barth et al., 2007; Pitcher et al., 2010).

3.5. Conclusions

To investigate the effects of surface heating on coastal upwelling intensity, simplified three-dimensional numerical experiments were conducted. Offshore transport, isopycnal slope, and the SST difference between coastal and offshore regions were evaluated.

Surface heating decreases Ekman transport but increases Ekman pumping transport owing to the increase in the air-sea stability. However, surface heating does not change net offshore transport significantly.

The isopycnal slope increases as the wind speed increases and surface heating decreases. The change in isopycnal slope is more vulnerable to the change in surface heating under strong wind speed conditions. The regression coefficients from the linear regression of isopycnal slope versus net surface heat flux are $-0.26 \pm 0.07\text{x}10^{-3}$, $-0.48 \pm 0.11\text{x}10^{-3}$, $-0.78 \pm 0.14\text{x}10^{-3}$, $-1.20 \pm 0.23\text{x}10^{-3}$, and $-1.49 \pm 0.31\text{x}10^{-3}$ for wind speeds of 4, 5, 6, 7, and 8 m/s, respectively. Modeling experiments demonstrate that H_{SBL} is crucial in determining the isopycnal slope. Surface heating, which forms a thinner SBL, results in a gentle isopycnal slope.

The SST difference between coastal and offshore regions

increases as the wind speed increases, as with the isopycnal slope. However, the SST difference also increases as the surface heating increases. The change in SST difference is more susceptible to the change in surface heating under weak wind speed conditions. The regression coefficients from the linear regression of SST difference versus net surface heat flux are $1.54 \pm 0.21\text{x}10^{-3}$, $1.40 \pm 0.29\text{x}10^{-3}$, $1.16 \pm 0.34\text{x}10^{-3}$, $0.87 \pm 0.30\text{x}10^{-3}$, and $0.63 \pm 0.25\text{x}10^{-3}$ for wind speeds of 4, 5, 6, 7, and 8 m/s, respectively. Model results suggested that vertical diffusion plays a key role in determining SST in the offshore region, but advection becomes impactful in the coastal region. Surface heating has two opposing effects on the SST difference. The SST difference decreases with an increase in the net surface heat flux in the coastal region but increases because of the advection induced by enhanced offshore velocity in the SBL simultaneously.

Both the H_{SBL} and offshore velocity in the SBL are closely related to the vertical eddy viscosity, which, in turn, depends on the mixing length and Ri. When the surface heating is weak, the vertical eddy viscosity increases and forms a thicker SBL which reduces the offshore velocity of the SBL. The isopycnal slope becomes steep because of the thick SBL, whereas the SST difference decreases

because of the reduced offshore velocity. When the surface heating is strong, it inhibits vertical mixing, and the vertical eddy viscosity decreases and forms a thinner SBL, resulting in an enhanced offshore velocity. The isopycnal slope becomes gentle because of the thin SBL, and the SST difference increases because of the enhanced offshore velocity despite the same offshore transport. The increase in the SST difference due to the enhanced offshore velocity overwhelms the decrease in the SST difference by net surface heat flux.

Although this study focused on local stratification, the findings of this study could be beneficial for studying larger and longer timescale implications concerning global warming in the future. The effect of surface heating could affect the upwelling source depth and flushing time of the subsurface in a coastal upwelling region, which affects the coastal ecosystem. Hence, additional research, including observations, is necessary to better understand the effect of surface heating on coastal upwelling.

4. Coastal wind-driven asymmetric circulation over a bank and effects of offshore currents

4.1. Introduction

The primary driving mechanism of the coastal circulation is the alongshore wind stress, and the wind-driven coastal circulation has been widely investigated (Allen, 1980; Brink, 1987; Huyer et al., 1978; Winant, 1980). In addition to alongshore wind stress, the presence of alongshore topographic variations also has a pronounced influence on coastal circulation (Gan and Allen, 2002; Saldías and Allen, 2020; Su and Pohlmann, 2009).

One of the alongshore topographic variations is banks. Many previous studies have attempted to understand the wind-driven coastal circulation over the bank (Barth et al., 2005; Castelao and Barth, 2006b; Kosro, 2005; Whitney and Allen, 2009a). Over the bank region, the response to the alongshore wind stress can vary depending on the shelf width, and a strong relationship exists between wind stress and alongshore currents over the upwind side (upwelling-favorable wind) of the bank (Kosro, 2005). In addition, the alongshore pressure gradient (APG) induced by preexisting upwelling jets can drive coastal circulation during wind relaxation

(Barth et al., 2005). Wind strength and bank geometry can modulate the separation of coastal upwelling jets (Castelao and Barth, 2006b). The separated upwelling jet is strongest over the upstream bank half, whereas the downwelling jet is symmetric about the bank center (Whitney and Allen, 2009a). Although there have been many studies on coastal circulation over banks, the causes of changes in the spatial structure are poorly understood. In addition, previous studies did not focus much on the effects of preexisting offshore currents.

In many cases, currents over coastal regions can be considered independent of offshore forcing (Allen, 1980). However, previous studies have suggested that offshore forcing plays an important role in coastal circulation (Awaji et al., 1991; Bane Jr et al., 1988; Hinata et al., 2008; Isoda, 1996; Oey, 1995; Palma et al., 2008; Park and Nam, 2018).

The southern sea region off the Korean Peninsula has a mean depth of approximately 100 m and bank-like topography (Fig. 4.1). There is an eastward alongshore currents throughout the year (Pang et al., 2003; Teague et al., 2003). During April to November 2019, surface currents were observed at six stations (dots in Fig. 4.1). The observational results showed a larger variability over the upstream part of the bank than over the downstream part of the bank (Fig.

4.3b). This asymmetric coastal response can excite coastal-trapped waves (Allen, 1980; Brink, 1991) which affect alongshore coastal currents (Park and Nam, 2018) and subtidal sea level fluctuations (Lee et al., 2022) around the Korean Peninsula. However, the cause of this asymmetric response has not yet been elucidated. This can be intrinsic variability over a bank region or induced by the effects of offshore currents.

In this study, the cause of the asymmetric coastal ocean response over the bank region and the effects of offshore currents were investigated by observational data analyses and numerical modeling. This chapter proceeds as follows: In section 4.2, the analysis methods, observational data, and numerical model configuration are described. Section 4.3 describes the asymmetric response over the bank, including the momentum balance. Section 4.4 is a discussion of the causes of the asymmetric response over the bank and the effects of offshore currents. Section 4.5 presents the conclusions from this study.

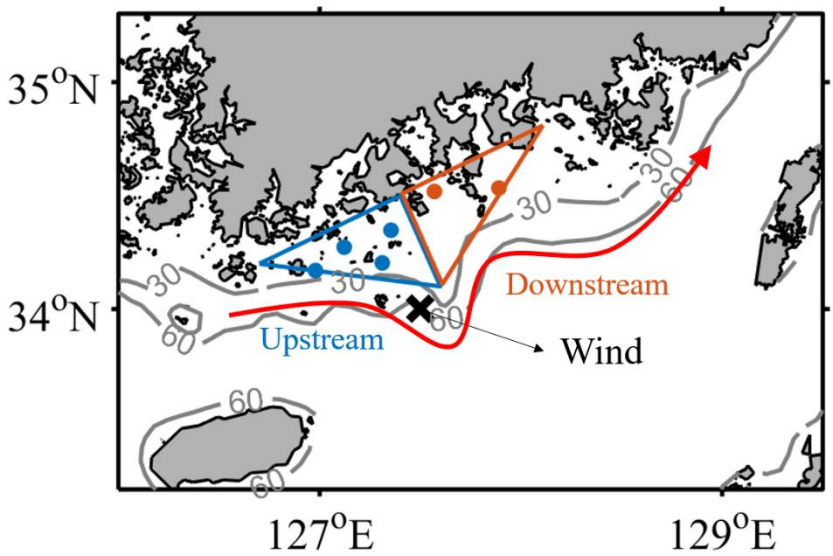

Figure 4.1 Observation stations (dots) for currents with bathymetry in the study area. Blue and red colors indicate the upstream and downstream regions of the bank. The gray lines represent 30-m and 60-m isobath. The red arrow is a schematic path of offshore currents.

4.2. Data and methods

In this study, the alongshore direction was defined as 20° counterclockwise from the west-east direction (positive eastward). All results from the observations and realistic model were 2-10 day band-pass filtered to focus on wind-driven coastal variability (Allen, 1980; Barth et al., 2005).

4.2.1. Observations

The surface current datasets (blue and orange dots in Fig. 4.1) are the results of tidal observations conducted by the Korea Hydrographic and Oceanographic Agency over 240 days. The depths of the observation stations were 28.5 m, 16.5 m, 28 m, 17.5 m, 10.5 m, and 24 m from the west (dots in Fig. 4.1). The wind datasets were obtained from the Geomundo buoy (black cross in Fig. 4.1) which has been maintained by the Korea Meteorological Administration.

4.2.2. Realistic model

The numerical model applied in this study was the Regional Ocean Modeling System (ROMS) (Shchepetkin and McWilliams, 2005), which is a split-explicit, free-surface, hydrostatic ocean model characterized by a terrain-following curvilinear system. The model domain was the same as that used in Chapter 2, but with a less smooth coastline and bottom topography on the southern coast of the Korean Peninsula. The model grid had a horizontal resolution of 6-8 km, and 40 vertical layers. KorBathy30s (Seo, 2008) and ETOPO1 (Amante, 2009) data were used for bottom topography, with a

minimum depth of 7 m. Initial temperature and salinity data were obtained from the result of Jung and Cho (2020). HYCOM GOFS 3.1 analysis data were adopted for the open boundary (https://www.hycom.org/dataserver/gofs-3pt1/analysis). The 6 hourly data from the European Centre for Medium-Range Weather Forecasts (ECMWF) ERA5 reanalysis were used for surface forcing, including air temperature, surface wind, air pressure, and relative humidity (C3S, 2017). Daily mean values were used for the precipitation and solar radiation. A bulk-flux formulation was used to calculate surface flux (Fairall et al., 1996). Tidal forcing was ignored to focus on the intrinsic dynamic response of the wind-driven coastal current over the bank. Discharges from 12 rivers were included. The monthly mean discharges at the Datong gauging station were used for the Changjiang River, and the river discharges of the other 11 rivers were obtained from the Global River Discharge Database (Vorosmarty et al., 1998). The K-profile parameterization mixing scheme was used for vertical mixing (Large et al., 1994). Chapman, Flather, and clamped boundary conditions were used for the free-surface, barotropic, and baroclinic momentums, respectively (Marchesiello et al., 2001). The horizontal viscosity coefficient was set as $100\,m^2s^{-1}$. The model was integrated for four

years (from 2016 to 2019), and the model results from 2019 were analyzed.

4.2.3. Idealized model

Because the complex coastline and bottom topography preclude dynamic analyses of the intrinsic variability over the bank region, idealized numerical experiments with a simplified coastline and bottom topography were conducted. The model domain was 500 km long and 200 km wide (Fig. 4.2a), with a grid resolution of 1 km horizontally, and 30 vertical layers. To precisely capture the surface boundary structure, fine vertical grid spacing (approximately 1 m) was implemented near the surface.

The idealized bank topography was formed by linear interpolation using the depths at the coast (0 m), 30 m isobath, and 100 km offshore (120 m) at each x−point.

The y−point of 30 m isobath ($y30$) is defined as follow:

$$y30(x) = y_{coast} - y_w \exp\left(-\left(\frac{x-x_m}{x_{ef}}\right)^2\right), \qquad (4.1)$$

where the values of y_{coast}, y_w, x_m, and x_{ef} were 199, 40, 250, and 50, respectively. The width and length of the bank are determined using y_w and x_{ef}. A minimum depth of 10 m is applied. The bank

geometry is of the same scale as that of the bank on the southern coast of the Korean Peninsula (Fig. 4.1).

Vertical mixing was calculated using the MY−2.5 turbulent closure scheme (Mellor and Yamada, 1982). The background vertical eddy viscosity and diffusivity were set to $10^{-5}\,m^2s^{-1}$. The Coriolis parameter, $f = 10^{-4}\,s^{-1}$, was utilized. The northern boundary was closed; the eastern and western boundaries were configured under periodic boundary conditions. At the offshore boundary, radiation was utilized for surface elevation. A Flather condition was applied to the barotropic momentums. Zero gradient conditions were used for baroclinic momentums and other 3D variables. The horizontal viscosity coefficient was set to 20 m^2s^{-1}, and the diffusivity coefficient was set to 2 m^2s^{-1} (Ledwell et al., 1998). The initial temperature as a function of the depth is as follows:

$$T(z) = 5 \times arctan\left(\frac{z+25}{15}\right) + 21, \qquad (4.2)$$

which represents a typical summer temperature profile on the southern coast of the Korean Peninsula. Salinity was set to a constant value of 32 during the experiments. The model was forced with a spatially uniform alongshore wind stress (Fig. 4.2b). The maximum wind stress (0.05 N/m^2) and period (8 day) of wind forcing were adapted based on the power spectrum analysis of the wind

observation datasets (black cross in Fig. 4.1). There is no surface heat flux.

In the experiments with offshore currents, a constant alongshore pressure gradient (1/250 hPa/km) was imposed as a body force (Zhang et al., 2011) to maintain the alongshore offshore flow, similar to the southern coast of the Korean Peninsula. After 30 days of spin-up without surface wind stress, the resultant offshore currents flowed along the isobath and reached a speed of approximately 30 cm/s near the bank head.

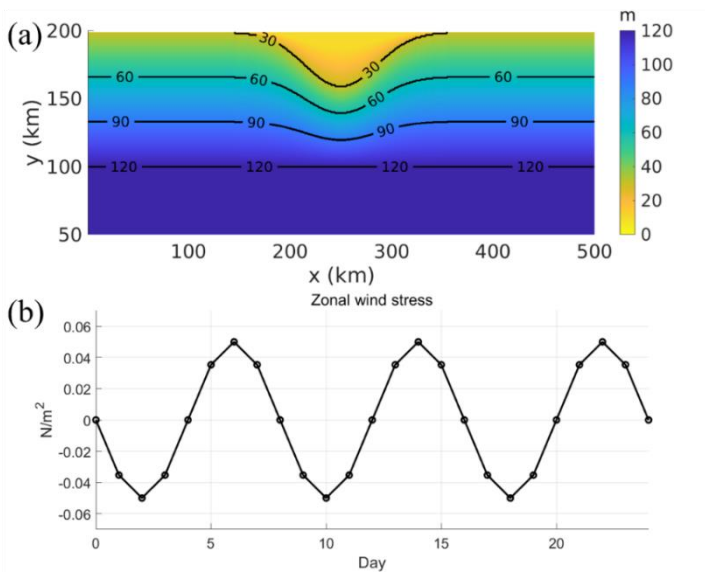

Figure 4.2 (a) Domain and bathymetry of idealized model. (b) Time series of alongshore wind stress applied to the idealized model experiments.

4.3. Results

4.3.1. Asymmetric response of coastal ocean

The alongshore wind and surface currents from observations and a realistic model during the summer of 2019 are shown in Fig. 4.3. In both the observations and model, the alongshore surface currents correlated well with the alongshore wind. The alongshore currents over the upstream half (blue lines in Fig. 4.3) were more susceptible to changes in the alongshore wind. This large variability in the upstream part of the bank can also be observed in the depth-averaged current over the upstream half of the area (Fig. 4.3d).

The model calculated daily mean depth-averaged alongshore currents on August 22 and September 6 (black dashed lines in Fig. 4.3d) are shown in Fig. 4.4. The speed of the alongshore currents over the upstream part of the bank (black dashed circles in Fig. 4.4) was greater than that over the downstream part of the bank during both westerly and easterly winds.

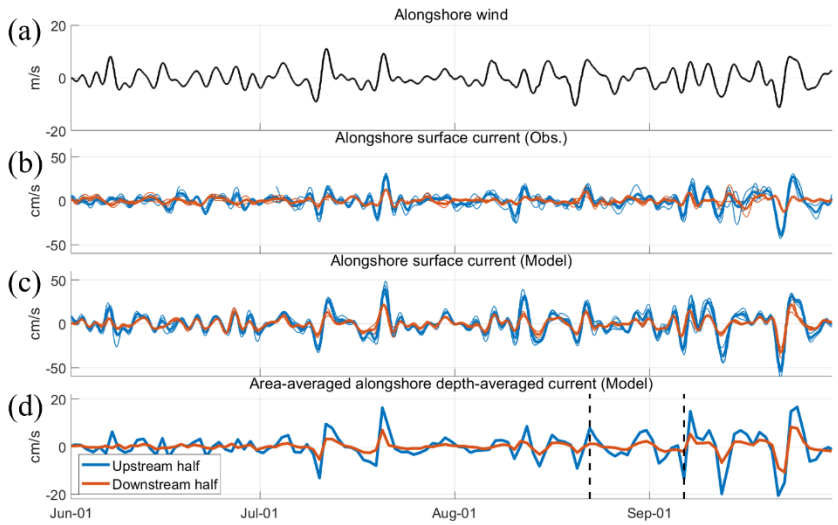

Figure 4.3 Timeseries of (a) alongshore wind, points-averaged alongshore surface currents from (b) observation and (c) realistic model, and (d) area-averaged (triangles in Fig. 4.1) alongshore depth-averaged currents from numerical model.

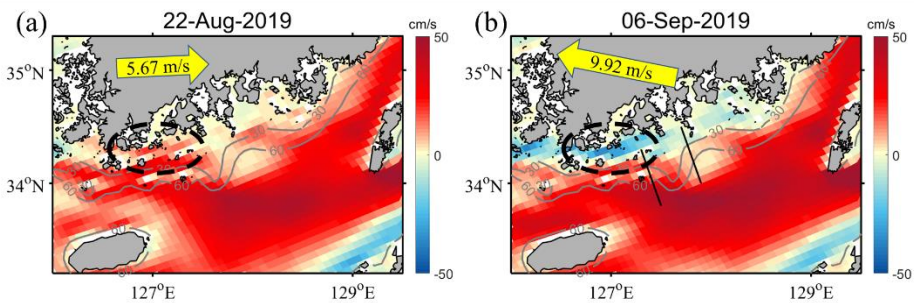

Figure 4.4 Daily mean depth-averaged alongshore currents from the realistic model on August 22, and September 6. The yellow arrows represent wind speed and approximate direction at the wind observation station (black cross in Fig. 4.1)

Time–latitude diagrams of the depth–averaged velocities along the black lines in Fig. 4.4b are shown in Fig. 4.5. In regions deeper than 60 m, the alongshore currents showed no significant differences between the upstream and downstream parts of the bank. However, in regions shallower than 30 m, the alongshore currents were more variable over the upstream region than over the downstream region.

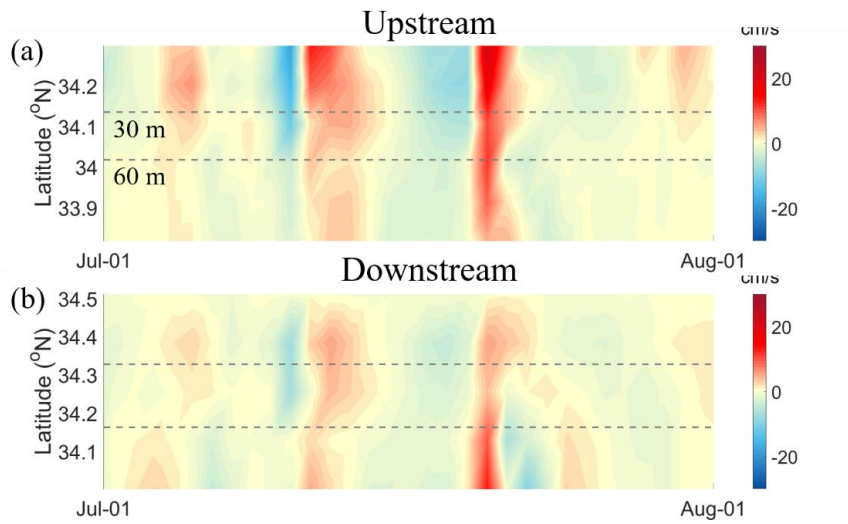

Figure 4.5 Time–latitude diagrams of depth–averaged alongshore currents from the realistic model in July 2019 along the black lines in Fig. 4.4b.

4.3.2. Momentum balance

The alongshore and cross–shore momentum balances along the

black lines in Fig. 4.4d were calculated to investigate the cause of large variability in the upstream part of the bank. The alongshore and cross-shore momentum balances in July averaged over a region shallower than 30 m are shown in Figs. 4.6 and 4.7.

In the alongshore direction, the alongshore currents were accelerated by the alongshore surface stress over the upstream part of the bank (Fig. 4.6a). However, over the downstream region, the alongshore pressure gradient force (PGF) developed counter to the alongshore surface stress, and no significant acceleration was observed.

In the cross-shore direction, the surface stress, the Coriolis force, and PGF were balanced. While the surface stress showed no significant difference between the upstream and downstream regions, the Coriolis force and PGF over the upstream region were much stronger than those over the downstream region, resulting in faster alongshore currents over the upstream region.

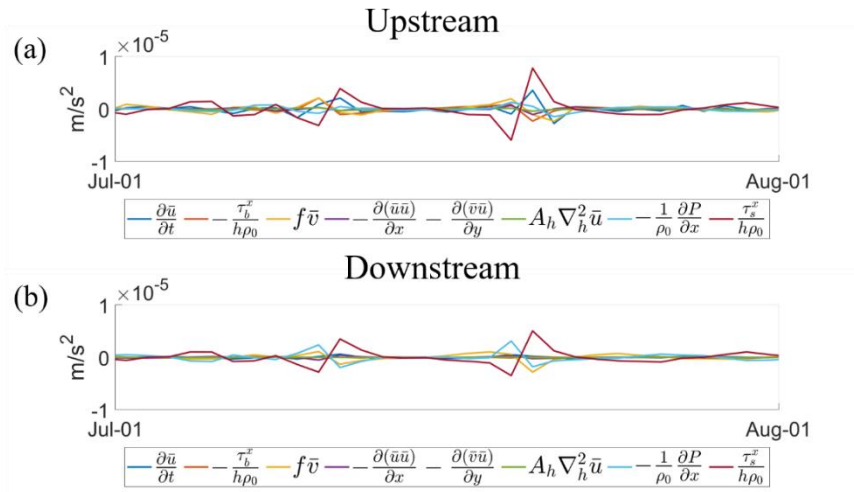

Figure 4.6 Alongshore momentum balance terms from the realistic model in July 2019 over the (a) upstream, and (b) downstream parts of the bank.

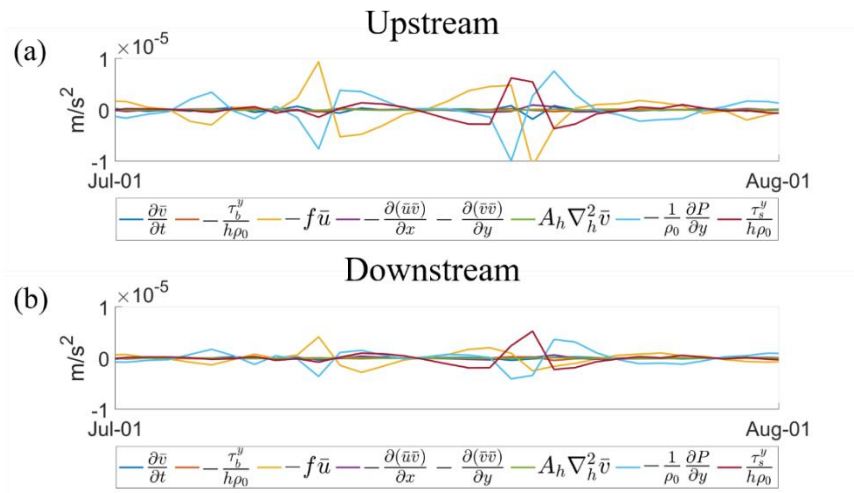

Figure 4.7 Cross-shore momentum balance terms from the realistic model in July 2019 over the (a) upstream, and (b) downstream parts of the bank.

4.4. Discussion

The alongshore momentum balance terms showed that the alongshore surface stress was offset by the alongshore PGF over the downstream part of the bank (Fig. 4.6b). This alongshore PGF may be induced by alongshore topographic variations in coastal regions (Gan and Allen, 2002; Rosenfeld et al., 1994; Su and Pohlmann, 2009). The results of the idealized model with a simplified coastline and bottom topography show that the alongshore currents over the upstream part of the bank have larger variability than those over the downstream part of the bank, as in the realistic model (Fig. 4.8 and 4.9). Sea level anomalies in the case of easterly (westerly) winds show an asymmetric sea level rise (depression) concentrated on the upstream part of the bank. This sea level distribution can induce alongshore PGF, which develops counter to the alongshore wind direction over the downstream region and stronger cross-shore PGF over the upstream region (Fig. 4.10). The idealized model results suggest that changes in the alongshore currents, cross-shore PGF, and alongshore PGF have the intrinsic variability over the bank region.

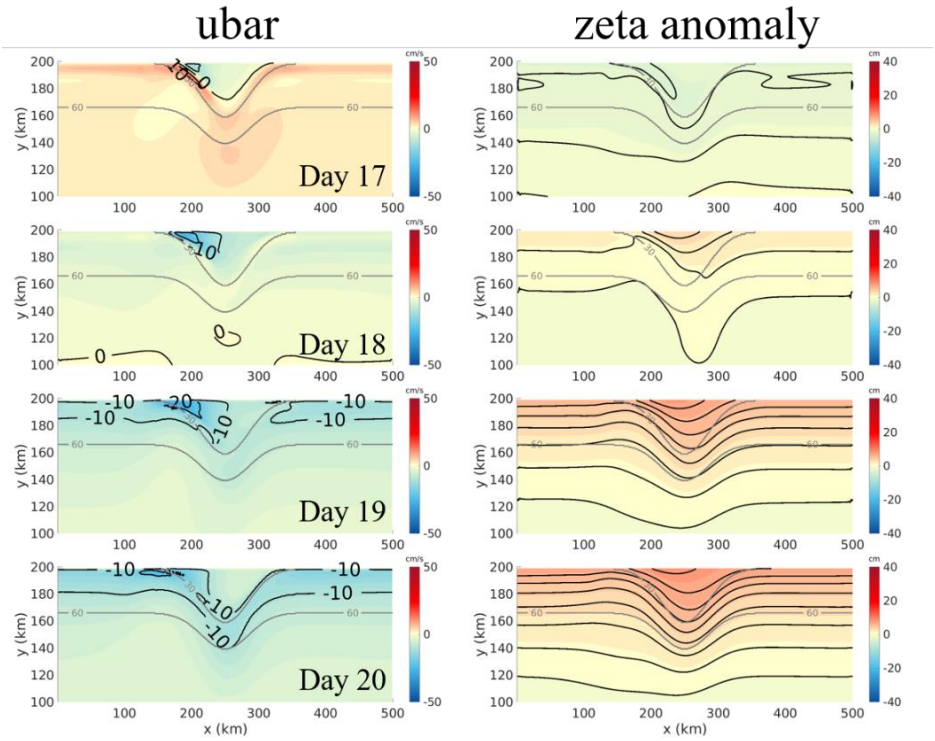

Figure 4.8 Daily mean of depth-averaged alongshore velocities (ubar, left) and sea level anomalies (zeta anomaly, right) from the idealized model from day 17 to day 24 (easterly) in Fig. 4.2. The contour intervals in sea level anomalies are 1 cm.

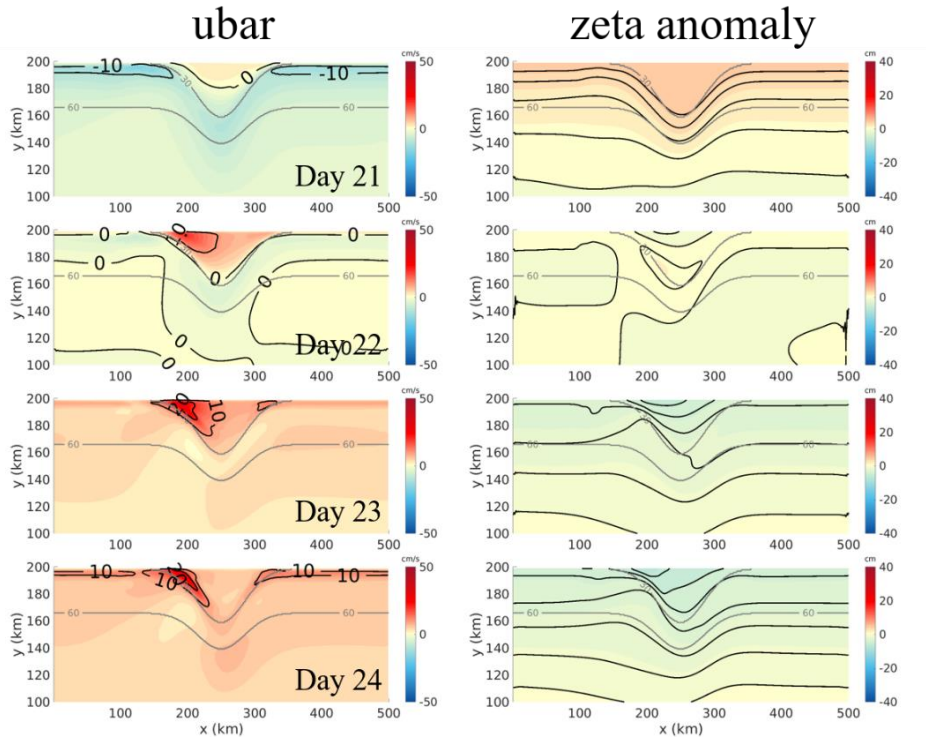

Figure 4.9 Same as Fig. 4.8 but from day 21 to day 24 (westerly).

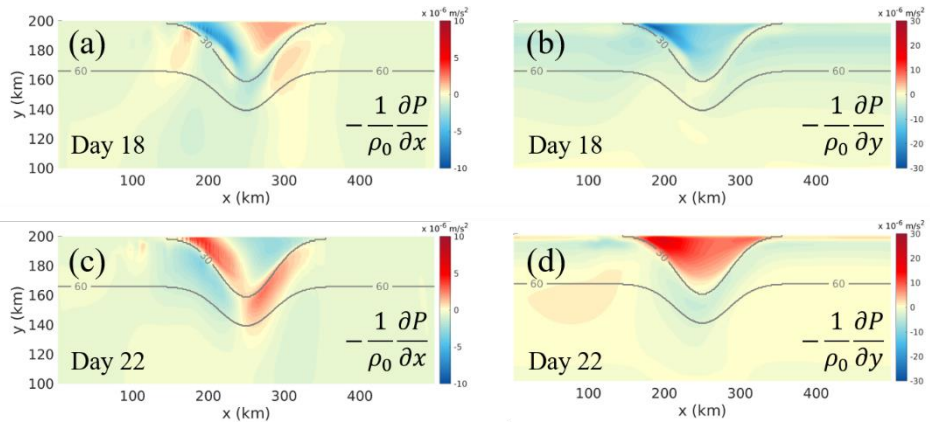

Figure 4.10 Alongshore (left) and cross-shore (right) pressure gradient forces from the idealized model on day 18 (a, b) and day 22 (b, d).

The asymmetric distribution of sea level over the bank region can be explained by differences in ageostrophic motion. When easterly and westerly winds blow, the ageostrophic motions in the shallow region (Fig. 4.11b and 4.11e) exhibit a greater magnitude and more directional response than those in the deeper region. This is because of the difference in the depth-averaged surface stress despite having the same surface wind stress. The difference in ageostrophic motionss according to depth can induce mass convergence or divergence, which results in an asymmetric distribution of sea level concentrated on the upstream part of the bank.

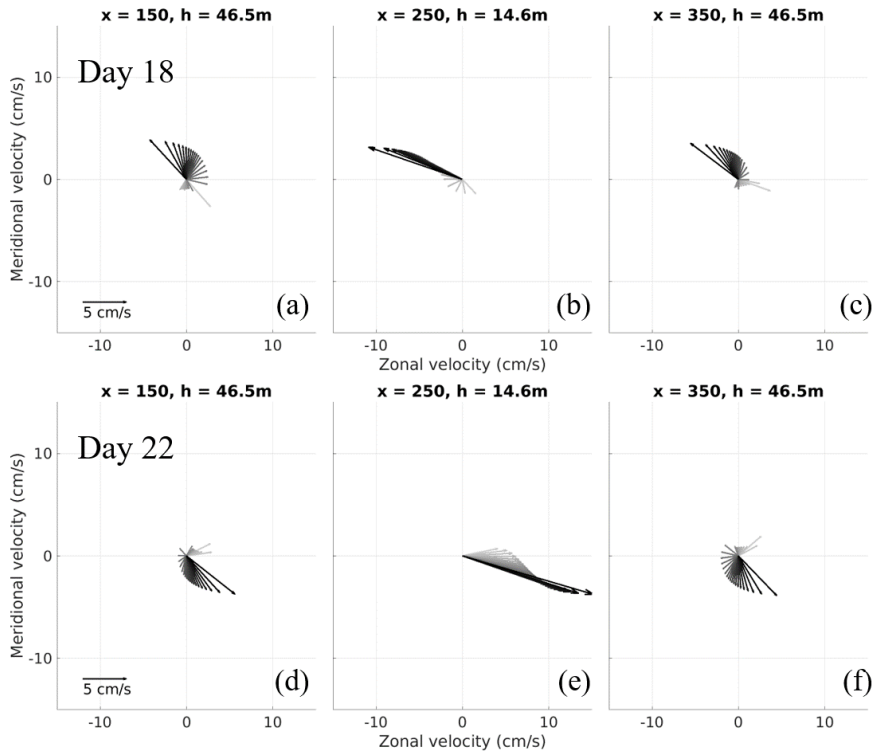

Figure 4.11 Ageostrophic currents vector at the west offshore area (left), bank center (middle), and east offshore area (right) of the idealized model on (top) day 18 (easterly peak) and (bottom) day 22 (westerly peak). Black color represents the surface layer.

The effects of offshore currents were investigated by applying them to an idealized model. In the case of the easterly winds, the westward currents over the upstream part of the bank propagate westward over time without offshore currents, and a downwelling jet is formed along the 30 m isobath (left column in Fig. 4.8). However, with offshore currents, the westward currents are confined to a shallow region (left column in Fig. 4.12). In addition, the westward

currents lingered over the upstream part of the bank and even propagated eastward (left column in Fig. 4.12). The main difference in sea level anomalies is the formation of the sea level minimum near the bank head (right column in Fig. 4.12). Without offshore currents, the water piles up raising the sea level northward (right column in Fig. 4.8). However, with offshore currents, a sea level minimum is formed between the piled-up water and the preexisting high sea level in the offshore region (right column in Fig. 4.12). These characteristics of alongshore currents and sea level distribution can also be observed in the results of the realistic model (Fig. 4.14). In the case of westerly winds, the eastward currents over the upstream part of the bank propagate southeastward and an upwelling jet is formed over time (left column in Fig. 4.9). With the offshore currents, the eastward currents were faster and gradually merged with the preexisting offshore currents resulting in an intensified upwelling jet (left column in Fig. 4.13). The preexisting high sea level in the offshore region makes the asymmetry in sea level distribution over the bank more prominent compared to that without offshore currents (right column in Fig. 4.13).

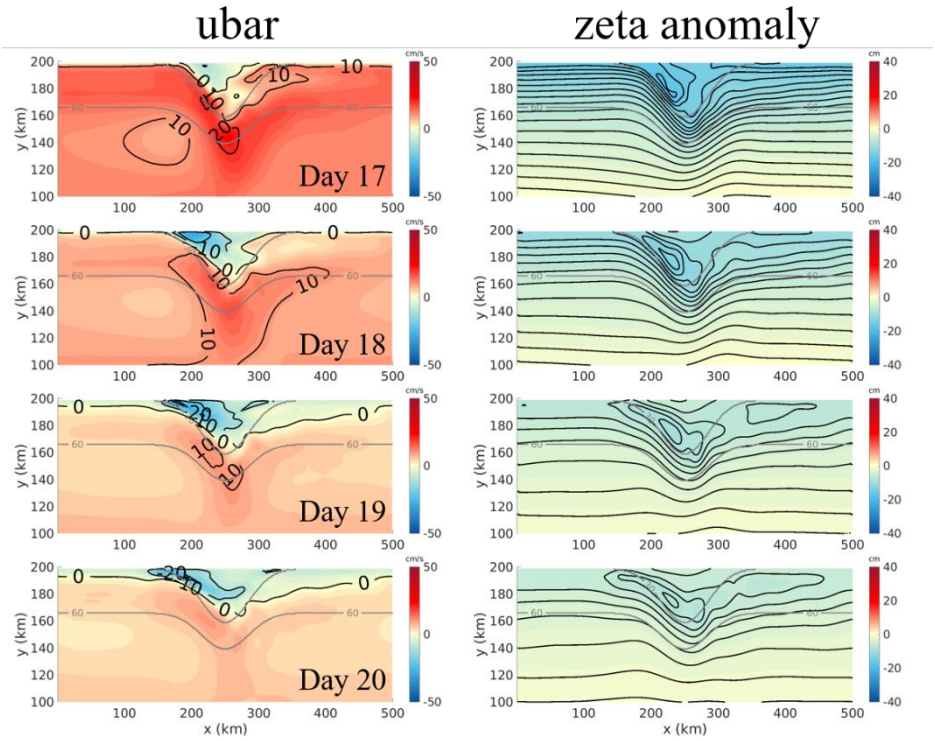

Figure 4.12 Daily mean of depth-averaged alongshore velocities (ubar, left) and sea level anomalies (zeta anomaly, right) calculated by the idealized model with offshore currents from day 17 to day 24 (easterly) in Fig. 4.2. The contour intervals in sea level anomalies are 1 cm.

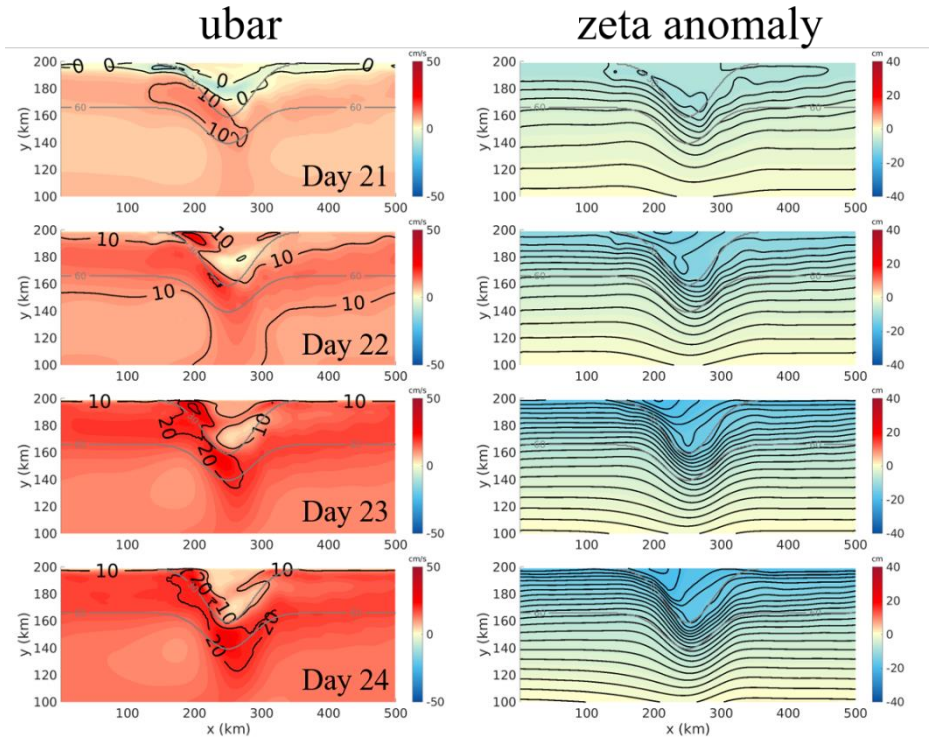

Figure 4.13 Same as Fig. 4.12 but from day 21 to day 24 (westerly).

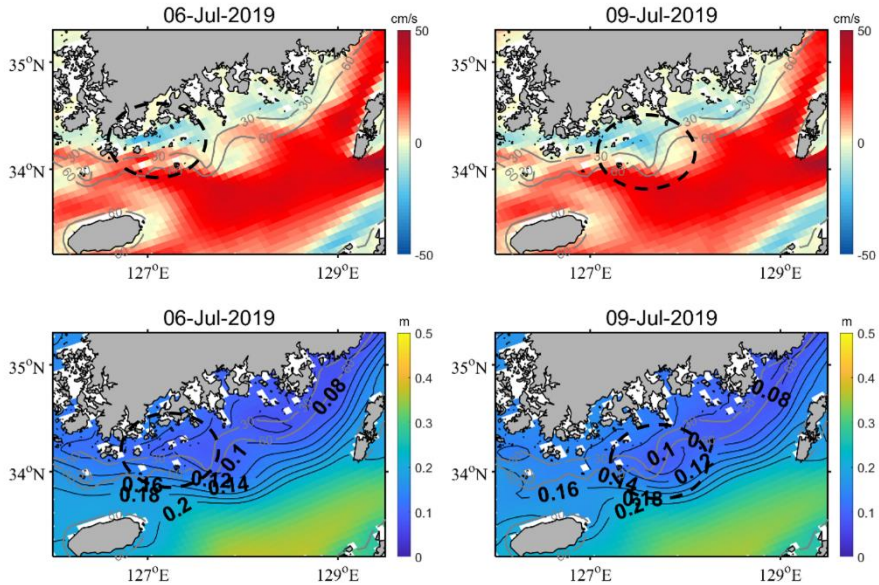

Figure 4.14 Daily means of depth-averaged alongshore velocities and sea levels from the realistic model on July 6, and July 9, 2019. Black dashed circles represent the eastward propagation of westward currents and sea level minimum over the bank center.

Transient wind forcing based on power spectrum analysis of the wind observation datasets was used for idealized experiments. With a longer duration of wind forcing, the upwelling or downwelling jet is fully developed along the isobath and becomes unstable due to baroclinic instability (Brink, 2016; Brink and Seo, 2016; Zhurbas et al., 2006). The bank geometry, including bank dimensions and geometric asymmetry, can affect the location of upwelling or downwelling jet (Castelao and Barth, 2006b; Whitney and Allen, 2009a, 2009b). However, the asymmetric distributions of the

alongshore velocities and sea level over the bank remain qualitatively unchanged because they are induced by differences in ageostrophic motion, which depends on the depth-averaged surface stress.

Where the preexisting alongshore currents can disturb the circulation over the bank, the increased magnitude of alongshore velocities over the upstream part of the bank according to the change in wind direction may not be observed (Barth et al., 2005). Instead, a stronger response of the surface currents to changes in the alongshore wind was still observed over the upstream part of the bank (Kosro, 2005).

4.5. Conclusions

The asymmetric response of the alongshore currents over the bank was reported using observational data measured in 2019. The alongshore currents over the upstream part of the bank have a larger variability than those over the downstream part, according to the change in the alongshore wind. The results of this study suggest that the main cause of the asymmetry in alongshore currents and sea level distribution is the difference in ageostrophic motion, which depends on the depth-averaged surface stress.

Offshore currents significantly affect alongshore circulation over the bank. In the case of easterly winds, the westward currents linger over the upstream part of the bank and even propagate eastward owing to the effect of offshore currents. The sea level distribution shows a sea level minimum near the bank head. In the case of westerly winds, the offshore currents intensify the asymmetry in alongshore currents and sea level distribution.

In the real ocean, a larger magnitude of alongshore velocities over the upstream part of the bank may not be observed, where preexisting offshore currents directly disturb the circulation over the bank. Instead, a more sensitive response to the change in the alongshore wind can be observed over the upstream part of the bank.

5. Summary and conclusions

To investigate the oceanic response to changes in wind and surface heating off the southern coast of the Korean Peninsula, observational data analyses and numerical modeling were performed.

Unprecedented coastal upwelling off the southern coast of the Korean Peninsula was reported during the summer of 2013. Observational data and numerical modeling results showed that upwelling occurred because of upwelling-favourable wind and persisted despite the weakening of the wind. Positive feedback between dynamic uplift and geostrophic adjustment maintained the coastal upwelling. Wind-driven coastal upwelling lowered the sea level, which enhanced the alongshore surface currents because of the increased cross-shore sea level difference. Strong alongshore surface currents maintained the dynamic uplift of cold, deep water in the coastal region by the geostrophic equilibrium.

The effects of surface heating on coastal upwelling intensity were investigated using simplified three-dimensional numerical experiments. Surface heating decreases Ekman transport but increases Ekman pumping transport owing to the increased air-sea stability. However, the net offshore transport did not change

significantly. Surface heating, which formed a thinner SBL, resulted in a gentle isopycnal slope. The SST difference decreases with an increase in the net surface heat flux in the coastal region but simultaneously increases because of the advection induced by the enhanced offshore velocity in the SBL. Both the SBL thickness and offshore velocity in the SBL are closely related to vertical eddy viscosity. When the surface heating was strong, the vertical eddy viscosity decreased and a thinner SBL was formed, resulting in an enhanced offshore velocity. The isopycnal slope became gentler because of the thin SBL, and the SST difference increased because of the enhanced offshore velocity. The increase in the SST difference owing to the enhanced offshore velocity overwhelmed the decrease by net surface heat flux.

Over the bank region, the asymmetric response of alongshore currents to changes in alongshore winds was reported using observational data in 2019. The alongshore currents over the upstream part of the bank showed greater variability than those over the downstream part. The main cause of this asymmetry is the difference in ageostrophic motion, which depends on the depth-averaged surface stress. The existence of offshore currents significantly affects the alongshore circulation over the bank. With

the offshore currents, the westward currents over the upstream part of the bank linger and propagate eastward in the case of easterly. The sea level distribution shows a sea level minimum near the bank head. On the other hand, in the case of westerly, the offshore currents strengthen the asymmetry in alongshore currents and sea level distribution.

The findings of this study provide insights into the physical processes occurring off the southern coast of the Korean Peninsula and their potential impacts on the coastal ecosystem. Unprecedented harmful algal blooms in the summer of 2013, caused by the combined effects of persistent strong winds and high air temperatures may occur frequently due to future global warming. Strong winds may facilitate harmful algal blooms by bringing nutrient-rich deep cold water to the surface. The dynamic mechanism of the relationship between upwelling and the nutrient supply will be investigated in future studies.

Although this study mainly focused on summer, the results of Chapters 2 and 3 can be applied to other seasons in which stratification occurs (spring to autumn). The results presented in Chapter 4 are applicable to all seasons as long as alongshore topographic variations exist. In addition, although this study

concentrated on the local oceanic response, its findings could be beneficial for studying other coastal areas of the world. The results presented in Chapter 2 can be applied to coastal areas where the alongshore geostrophic currents persist long after the weakening of the upwelling-favorable wind. The results of Chapter 3 are applicable to coastal regions where the effect of alongshore pressure gradient is not significant to upwelling system. Finally, the results presented in Chapter 4 can be applied to any coastal region where alongshore topographic variations exist.

Appendix

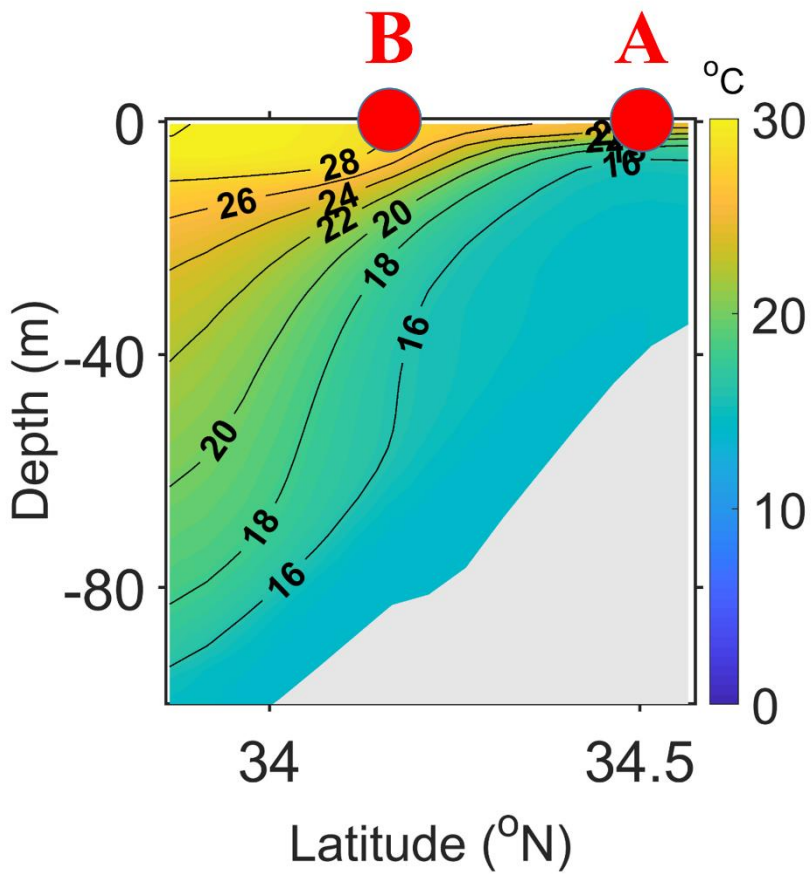

Figure A1 Model calculated cross-shore section of the August monthly mean temperatures along the red line in Fig. 2.1b.

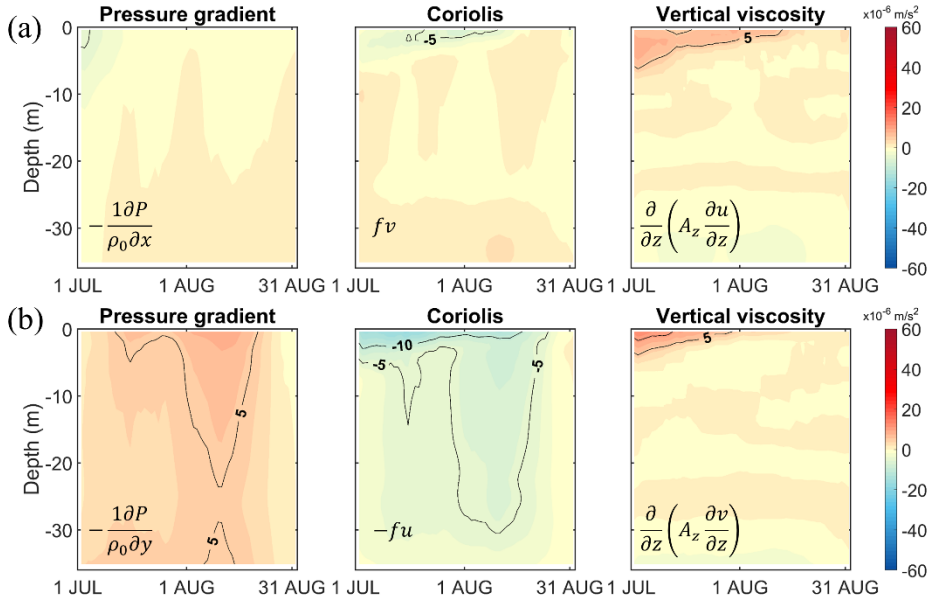

Figure A2 Time series of (a) alongshore momentum balance terms and (b) cross-shore momentum balance terms at the red dot A in Fig. A1. All terms are filtered by a 2-week running mean of the daily means.

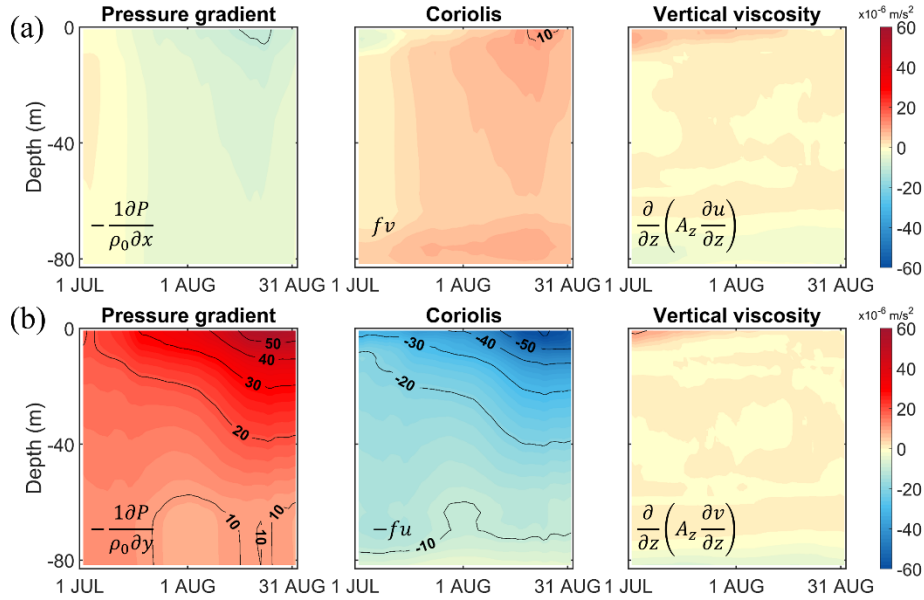

Figure A3 Time series of (a) alongshore momentum balance terms and (b) cross-shore momentum balance terms at the red dot B in Fig. A1. All terms are filtered by a 2-week running mean of the daily means.

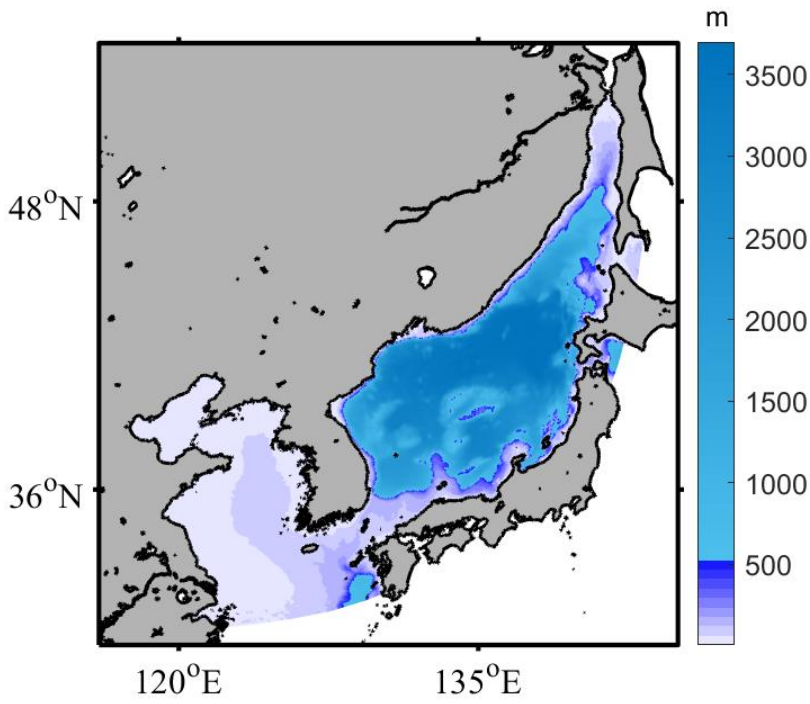

Figure A4 Domain of numerical model with bottom topography.

Bibliography

Allen, J., 1980: Models of wind-driven currents on the continental shelf. *Annual Review of Fluid Mechanics*, **12,** 389-433.

Allen, J., P. Newberger, and J. Federiuk, 1995: Upwelling circulation on the Oregon continental shelf. Part I: Response to idealized forcing. *Journal of Physical Oceanography*, **25,** 1843-1866.

Allen, J. S., 1973: Upwelling and coastal jets in a continuously stratified ocean. *Journal of Physical Oceanography*, **3,** 245-257.

Amante, C., 2009: ETOPO1 1 arc-minute global relief model: procedures, data sources and analysis. *http://www.ngdc.noaa.gov/mgg/global/global.html*.

Austin, J. A., and J. A. Barth, 2002: Variation in the position of the upwelling front on the Oregon shelf. *Journal of Geophysical Research: Oceans*, **107,** 1-1-1-15.

Austin, J. A., and S. J. Lentz, 2002: The inner shelf response to wind-driven upwelling and downwelling. *Journal of Physical Oceanography*, **32,** 2171-2193.

Awaji, T., K. Akitomo, and N. Imasato, 1991: Numerical study of shelf water motion driven by the Kuroshio: Barotropic model. *Journal of Physical Oceanography*, **21,** 11-27.

Bae, S.-W., and D.-S. Kim, 2012: Understanding the flow properties by a numerical modeling in the South Sea of Korea. *Journal of the Korean Society of Marine Environment & Safety*, **18,** 295-307.

Bane Jr, J. M., O. B. Brown, R. H. Evans, and P. Hamilton, 1988: Gulf Stream remote forcing of shelfbreak currents in the Mid-Atlantic Bight. *Geophysical research letters*, **15,** 405-407.

Barth, J. A., S. Pierce, and R. Castelao, 2005: Time-dependent, wind-driven flow over a shallow midshelf submarine bank. *Journal of Geophysical Research: Oceans*, **110**.

Barth, J. A., and Coauthors, 2007: Delayed upwelling alters nearshore coastal ocean ecosystems in the northern California current. *Proceedings of the National Academy of Sciences*, **104,** 3719-3724.

Benazzouz, A., and Coauthors, 2014: On the temporal memory of coastal upwelling off NW Africa. *Journal of Geophysical Research: Oceans*, **119,** 6356-6380.

Berliand, M., 1952: Determining the net long-wave radiation of the

Earth with consideration of the effect of cloudiness. *Izv. Akad. Nauk. SSSR Ser. Geofiz*, **1,** 64-78.

Bode, A., M. Alvarez-Ossorio, J. Cabanas, A. Miranda, and M. Varela, 2009: Recent trends in plankton and upwelling intensity off Galicia (NW Spain). *Progress in Oceanography*, **83,** 342-350.

Brink, K., 1991: Coastal-trapped waves and wind-driven currents over the continental shelf. *Annual Review of Fluid Mechanics*, **23,** 389-412.

——, 2016: Continental shelf baroclinic instability. Part I: Relaxation from upwelling or downwelling. *Journal of Physical Oceanography*, **46,** 551-568.

Brink, K., and H. Seo, 2016: Continental shelf baroclinic instability. Part II: Oscillating wind forcing. *Journal of Physical Oceanography*, **46,** 569-582.

Brink, K. H., 1987: Coastal ocean physical processes. *Reviews of Geophysics*, **25,** 204-216.

Byun, D.-S., and B. J. Choi, 2018: Nomenclature of the Seas Around the Korean Peninsula Derived From Analyses of Papers in Two Representative Korean Ocean and Fisheries Science Journals: Present Status and Future. *The Sea*, **23**.

Capet, X., P. Marchesiello, and J. McWilliams, 2004: Upwelling response to coastal wind profiles. *Geophysical Research Letters*, **31**.

Castelao, R. M., and J. A. Barth, 2006a: Upwelling around Cabo Frio, Brazil: The importance of wind stress curl. *Geophysical Research Letters*, **33,** L03602.

——, 2006b: The relative importance of wind strength and along-shelf bathymetric variations on the separation of a coastal upwelling jet. *Journal of physical oceanography*, **36,** 412-425.

Chelton, D. B., M. G. Schlax, and R. M. Samelson, 2007: Summertime coupling between sea surface temperature and wind stress in the California Current System. *Journal of Physical Oceanography*, **37,** 495-517.

Chen, Z., X.-H. Yan, Y. Jiang, and L. Jiang, 2013: Roles of shelf slope and wind on upwelling: A case study off east and west coasts of the US. *Ocean Modelling*, **69,** 136-145.

Chen, Z., J. Pan, Y. Jiang, and H. Lin, 2017: Far-reaching transport of Pearl River plume water by upwelling jet in the northeastern South China Sea. *Journal of Marine Systems*, **173,** 60-69.

Chen, Z., Y. Jiang, J. Wang, and W. Gong, 2019: Influence of a River Plume on Coastal Upwelling Dynamics: Importance of Stratification. *Journal of Physical Oceanography*, **49,** 2345-

2363.
Cho, Y.-K., and K. Kim, 1994: Characteristics and Origin of the Cold Water in the South Sea of Korea in Summer. *Journal of the Korean Society of Oceanography*, **29,** 414-421.
Cho, Y.-K., K. Kim, and H. K. Rho, 1995: Salinity Decrease and the Transport in the South Sea of Korea in Summer. *Journal of Korean Society of Coastal and Ocean Engineers*, **7,** 126-134.
Copernicus-Climate-Change-Service, 2017: ERA5: Fifth generation of ECMWF atmospheric reanalyses of the global climate . Copernicus Climate Change Service Climate Data Store (CDS), accessed: 2019. https://cds.climate.copernicus.eu/cdsapp#!/home.
Demarcq, H., and V. Faure, 2000: Coastal upwelling and associated retention indices derived from satellite SST. Application to Octopus vulgaris recruitment. *Oceanologica acta*, **23,** 391-408.
Djurfeldt, L., 1989: Circulation and mixing in a coastal upwelling embayment; Gulf of Arauco, Chile. *Continental Shelf Research*, **9,** 1003-1016.
Egbert, G. D., and S. Y. Erofeeva, 2002: Efficient inverse modeling of barotropic ocean tides. *Journal of Atmospheric and Oceanic Technology*, **19,** 183-204.
Ekman, V. W., 1905: On the influence of the earth's rotation on ocean-currents. *Arkiv för matematik, astronomi och fysik*, **2,** 1-52.
Enriquez, A., and C. Friehe, 1995: Effects of wind stress and wind stress curl variability on coastal upwelling. *Journal of Physical Oceanography*, **25,** 1651-1671.
Estrade, P., P. Marchesiello, A. C. De Verdière, and C. Roy, 2008: Cross-shelf structure of coastal upwelling: A two-dimensional extension of Ekman's theory and a mechanism for inner shelf upwelling shut down. *Journal of marine research*, **66,** 589-616.
Fairall, C. W., E. F. Bradley, D. P. Rogers, J. B. Edson, and G. S. Young, 1996: Bulk parameterization of air-sea fluxes for tropical ocean-global atmosphere coupled-ocean atmosphere response experiment. *Journal of Geophysical Research: Oceans*, **101,** 3747-3764.
Fairall, C. W., E. F. Bradley, J. Hare, A. A. Grachev, and J. B. Edson, 2003: Bulk parameterization of air-sea fluxes: Updates and verification for the COARE algorithm. *Journal of climate*, **16,** 571-591.
Forryan, A., A. P. Martin, M. A. Srokosz, E. E. Popova, S. C. Painter,

and A. H. Renner, 2013: A new observationally motivated Richardson number based mixing parametrization for oceanic mesoscale flow. *Journal of Geophysical Research: Oceans*, **118**, 1405–1419.

Gan, J., and J. S. Allen, 2002: A modeling study of shelf circulation off northern California in the region of the Coastal Ocean Dynamics Experiment: Response to relaxation of upwelling winds. *Journal of Geophysical Research: Oceans*, **107**, 6–1–6–31.

García–Reyes, M., J. L. Largier, and W. J. Sydeman, 2014: Synoptic–scale upwelling indices and predictions of phyto–and zooplankton populations. *Progress in Oceanography*, **120**, 177–188.

Gill, A., and A. Clarke, 1974: Wind–induced upwelling, coastal currents and sea–level changes. *Deep Sea Research and Oceanographic Abstracts*, Elsevier, 325–345.

Gong, Y., 1971: A study on the south korean coastal front. *The Journal of the Oceanological Society of Korea*, **6**, 25–36.

He, J., and A. Mahadevan, 2021: How the source depth of coastal upwelling relates to stratification and wind. *Journal of Geophysical Research: Oceans*, **126**, e2021JC017621.

Hinata, H., T. Yanagi, and C. Satoh, 2008: Sea level response to wind field fluctuation around the tip of the Izu Peninsula. *Journal of oceanography*, **64**, 605–620.

Hsueh, Y., and R. N. Kenney III, 1972: Steady coastal upwelling in a continuously stratified ocean. *Journal of Physical Oceanography*, **2**, 27–33.

Huyer, A., R. L. Smith, and E. J. Sobey, 1978: Seasonal differences in low-frequency current fluctuations over the Oregon continental shelf. *Journal of Geophysical Research: Oceans*, **83**, 5077–5089.

Isoda, Y., 1996: Interaction of a warm eddy with the coastal current at the eastern boundary area in the Tsushima Current region. *Continental Shelf Research*, **16**, 1149–1163.

Jacox, M., and C. Edwards, 2011: Effects of stratification and shelf slope on nutrient supply in coastal upwelling regions. *Journal of Geophysical Research: Oceans*, **116**.

——, 2012: Upwelling source depth in the presence of nearshore wind stress curl. *Journal of Geophysical Research: Oceans*, **117**.

Jacox, M. G., C. A. Edwards, E. L. Hazen, and S. J. Bograd, 2018: Coastal upwelling revisited: Ekman, Bakun, and improved upwelling indices for the US West Coast. *Journal of*

Geophysical Research: Oceans, **123,** 7332–7350.
Jin, X., C. Dong, J. Kurian, J. C. McWilliams, D. B. Chelton, and Z. Li, 2009: SST–wind interaction in coastal upwelling: Oceanic simulation with empirical coupling. *Journal of Physical Oceanography*, **39,** 2957–2970.
Jung, J., and Y.–K. Cho, 2020: Persistence of coastal upwelling after a plunge in upwelling–favourable wind. *Scientific reports*, **10,** 1–9.
Kämpf, J., and P. Chapman, 2016: Upwelling systems of the world: A scientific journey to the most productive marine ecosystems, Springer International Publishing, 433p.
Kang, C., 1974: A study on the seasonal variation of the water masses in the southern sea of Korea. *Bulletin of National Fisheries Research and Development Institute. Republic of Korea.*, **12,** 107–121.
Kara, A. B., H. E. Hurlburt, and A. J. Wallcraft, 2005: Stability–dependent exchange coefficients for air–sea fluxes. *Journal of Atmospheric and Oceanic Technology*, **22,** 1080–1094.
Kim, C.–K., K.–I. Chang, K. Park, and M.–S. Suk, 2000: The south sea circulation of korea: Two–dimensional barotrophic model. *The Sea: Journal of the Korean Society of Oceanography*, **5,** 257–266.
Kim, I.–O., and H. K. Rho, 1994: A study on China coastal water appeared in the neighbouring seas of Cheju Island. *Journal of the Korean Fisheries Society*, **27,** 515–528.
Kim, J.–K., B.–J. Choi, J. Kim, and Y.–J. Sun, 2022: Wind–driven retreat of cold water pool and abrupt sea temperature rise off the southwest coast of Korea in summer 2017. *Journal of Marine Systems*, **231,** 103739.
Kosro, P. M., 2005: On the spatial structure of coastal circulation off Newport, Oregon, during spring and summer 2001 in a region of varying shelf width. *Journal of Geophysical Research: Oceans*, **110.**
Kwoun, C. H., K. D. Cho, and D. S. Kim, 2002: A Numerical simulation for the circulation of sea water in the Southern Coastal Waters in Korea. *Journal of the Korean Society for Marine Environment & Energy*, **5,** 27–40.
Large, W. G., J. C. McWilliams, and S. C. Doney, 1994: Oceanic vertical mixing: A review and a model with a nonlocal boundary layer parameterization. *Reviews of Geophysics*, **32,** 363–403.
Ledwell, J. R., A. J. Watson, and C. S. Law, 1998: Mixing of a tracer in the pycnocline. *Journal of Geophysical Research: Oceans*,

103, 21499–21529.

Lee, K., S. Nam, and J. H. Park, 2022: Alongshore propagation of subtidal sea level fluctuations around the Korean Peninsula over varying stratification and shelf topography. *Frontiers in Marine Science*, **8**.

Lee, M., S. Lee, P. Kim, and B. Kim, 2018: Characteristics of water masses and its distributions in the southern coastal waters of Korea in summer. *Journal of the Korean Society for Marine Environment and Energy*, **21,** 76–96.

Lentz, S. J., 1995: Sensitivity of the inner–shelf circulation to the form of the eddy viscosity profile. *Journal of Physical Oceanography*, **25,** 19–28.

——, 2001: The influence of stratification on the wind–driven cross–shelf circulation over the North Carolina shelf. *Journal of Physical Oceanography*, **31,** 2749–2760.

Lentz, S. J., and D. C. Chapman, 2004: The importance of nonlinear cross–shelf momentum flux during wind–driven coastal upwelling. *Journal of Physical Oceanography*, **34,** 2444–2457.

Lie, H.–J., and C.–H. Cho, 2016: Seasonal circulation patterns of the Yellow and East China Seas derived from satellite–tracked drifter trajectories and hydrographic observations. *Progress in Oceanography*, **146,** 121–141.

Lim, D. B., 1976: The movements of the waters off the south coast of Korea. *The Journal of the Oceanological Society of Korea*, **11,** 77–88.

Locarnini, R. A., and Coauthors, 2019: World Ocean Atlas 2018, Volume 1: Temperature. A. Mishonov Technical Editor. *NOAA Atlas NESDIS*, **81,** 52pp.

Marcello, J., A. Hernandez–Guerra, F. Eugenio, and A. Fonte, 2011: Seasonal and temporal study of the northwest African upwelling system. *International Journal of Remote Sensing*, **32,** 1843–1859.

Marchesiello, P., and P. Estrade, 2010: Upwelling limitation by onshore geostrophic flow. *Journal of Marine Research*, **68,** 37–62.

Marchesiello, P., J. C. McWilliams, and A. Shchepetkin, 2001: Open boundary conditions for long–term integration of regional oceanic models. *Ocean modelling*, **3,** 1–20.

McCabe, R. M., B. M. Hickey, E. P. Dever, and P. MacCready, 2015: Seasonal cross–shelf flow structure, upwelling relaxation, and the alongshelf pressure gradient in the Northern California Current System. *Journal of Physical Oceanography*, **45,** 209–

227.
Mellor, G. L., and T. Yamada, 1982: Development of a turbulence closure model for geophysical fluid problems. *Reviews of Geophysics*, **20,** 851-875.
Munk, W. H., and E. Anderson, 1948: Note on a theory of the thermocline. *J. Mar. Res.*, **7,** 276-295.
Nishida, K., 1926: Report of the oceanographic investigation. No. 1. *Government Fishery Experimental Station*, 68 pp.
Nykjær, L., and L. Van Camp, 1994: Seasonal and interannual variability of coastal upwelling along northwest Africa and Portugal from 1981 to 1991. *Journal of Geophysical Research: Oceans*, **99,** 14197-14207.
Oey, L. Y., 1995: Eddy-and wind-forced shelf circulation. *Journal of Geophysical Research: Oceans*, **100,** 8621-8637.
Palma, E. D., R. P. Matano, and A. R. Piola, 2008: A numerical study of the Southwestern Atlantic Shelf circulation: Stratified ocean response to local and offshore forcing. *Journal of Geophysical Research: Oceans*, **113**.
Pang, I., C. Hong, K. Chang, J. Lee, and J. Kim, 2003: Monthly variation of water mass distribution and current in the Cheju Strait. *Journal of the Korean Society of Oceanography*, **38,** 87-100.
Park, J. H., and S. Nam, 2018: Causes of Interannual Variation of Summer Mean Alongshore Current Near the East Coast of Korea Derived From 16-Year-Long Observational Data. *Journal of Geophysical Research: Oceans*, **123,** 7781-7794.
Pedlosky, J., 1978: A nonlinear model of the onset of upwelling. *Journal of Physical Oceanography*, **8,** 178-187.
Pickett, M. H., and J. D. Paduan, 2003: Ekman transport and pumping in the California Current based on the US Navy's high-resolution atmospheric model (COAMPS). *Journal of Geophysical Research: Oceans*, **108**.
Pitcher, G., F. Figueiras, B. Hickey, and M. Moita, 2010: The physical oceanography of upwelling systems and the development of harmful algal blooms. *Progress in Oceanography*, **85,** 5-32.
Price, J. F., and M. A. Sundermeyer, 1999: Stratified ekman layers. *Journal of Geophysical Research: Oceans*, **104,** 20467-20494.
Rosenfeld, L. K., F. B. Schwing, N. Garfield, and D. E. Tracy, 1994: Bifurcated flow from an upwelling center: a cold water source for Monterey Bay. *Continental Shelf Research*, **14,** 931-964.
Roughan, M., and J. H. Middleton, 2004: On the East Australian Current: variability, encroachment, and upwelling. *Journal of*

Geophysical Research: Oceans, **109,** C07003.
Roughan, M., P. R. Oke, and J. H. Middleton, 2003: A modeling study of the climatological current field and the trajectories of upwelled particles in the East Australian Current. *Journal of Physical Oceanography*, **33,** 2551-2564.
Saldías, G. S., and S. E. Allen, 2020: The influence of a submarine canyon on the circulation and cross-shore exchanges around an upwelling front. *Journal of Physical Oceanography*, **50,** 1677-1698.
Send, U., and S. Nam, 2012: Relaxation from upwelling: the effect on dissolved oxygen on the continental shelf. *Journal of Geophysical Research: Oceans*, **117**.
Send, U., R. C. Beardsley, and C. D. Winant, 1987: Relaxation from upwelling in the coastal ocean dynamics experiment. *Journal of Geophysical Research: Oceans*, **92,** 1683-1698.
Seo, S.-N., 2008: Digital 30sec Gridded Bathymetric Data of Korea Marginal Seas - KorBathy30s. *Journal of Korean Society of Coastal and Ocean Engineers*, **20,** 110-120.
Seung, Y. H., 1992: Water Masses and Circulations around Korean Peninsula. *The Journal of the Oceanological Society of Korea*, **27,** 324-331.
Shchepetkin, A. F., and J. C. McWilliams, 2005: The regional oceanic modeling system (ROMS): a split-explicit, free-surface, topography-following-coordinate oceanic model. *Ocean Modelling*, **9,** 347-404.
Shen, M.-L., Y.-H. Tseng, and S. Jan, 2011: The formation and dynamics of the cold-dome off northeastern Taiwan. *Journal of Marine Systems*, **86,** 10-27.
Shi, W., J. M. Morrison, E. Böhm, and V. Manghnani, 2000: The Oman upwelling zone during 1993, 1994 and 1995. *Deep Sea Research Part II: Topical Studies in Oceanography*, **47,** 1227-1247.
Simpson, J., C. Allen, and N. Morris, 1978: Fronts on the continental shelf. *Journal of Geophysical Research: Oceans*, **83,** 4607-4614.
Simpson, J., E. Williams, L. Brasseur, and J. Brubaker, 2005: The impact of tidal straining on the cycle of turbulence in a partially stratified estuary. *Continental Shelf Research*, **25,** 51-64.
Smith, R. L., 1968: Upwelling. *Oceanography and Marine Biology: An Annual Review*, **6,** 1-46.
Smith, R. L., 1981: A comparison of the structure and variability of the flow field in three coastal upwelling regions: Oregon,

Northwest Africa, and Peru. *Coastal upwelling*, **1,** 107–118.
Spall, M. A., and N. Schneider, 2016: Coupled Ocean–Atmosphere Offshore Decay Scale of Cold SST Signals along Upwelling Eastern Boundaries. *Journal of Climate*, **29,** 8317–8331.
Strub, P. T., and Coauthors, 2015: Altimeter-derived seasonal circulation on the southwest A tlantic shelf: 27°–43° S. *Journal of Geophysical Research: Oceans*, **120,** 3391–3418.
Su, J., and T. Pohlmann, 2009: Wind and topography influence on an upwelling system at the eastern Hainan coast. *Journal of Geophysical Research: Oceans*, **114**.
Tapia, F. J., and Coauthors, 2009: Thermal indices of upwelling effects on inner–shelf habitats. *Progress in Oceanography*, **83,** 278–287.
Teague, W., G. Jacobs, D. Ko, T. Tang, K.–I. Chang, and M.–S. Suk, 2003: Connectivity of the Taiwan, Cheju, and Korea straits. *Continental Shelf Research*, **23,** 63–77.
Uda, M., 1934: The results of simultaneous oceanographic investigations in the Japan Sea and its adjacent waters in May and June, 1932. *Journal of the Imperial Fishery Experimental Stations*, **5,** 57–190.
Vorosmarty, C., B. Fekete, and B. Tucker, 1998: Global River Discharge, 1807–1991, V [ersion]. 1.1 (RivDIS). *ORNL DAAC*.
Walter, R. K., C. B. Woodson, P. R. Leary, and S. G. Monismith, 2014: Connecting wind-driven upwelling and offshore stratification to nearshore internal bores and oxygen variability. *Journal of Geophysical Research: Oceans*, **119,** 3517–3534.
Wang, D. P., 1997: Effects of small-scale wind on coastal upwelling with application to Point Conception. *Journal of Geophysical Research: Oceans*, **102,** 15555–15566.
Wenegrat, J. O., and M. J. McPhaden, 2016: A simple analytical model of the diurnal Ekman layer. *Journal of Physical Oceanography*, **46,** 2877–2894.
Whitney, M. M., and J. Allen, 2009a: Coastal wind–driven circulation in the vicinity of a bank. Part I: Modeling flow over idealized symmetric banks. *Journal of physical oceanography*, **39,** 1273–1297.
——, 2009b: Coastal wind–driven circulation in the vicinity of a bank. Part II: Modeling flow over the Heceta Bank complex on the Oregon coast. *Journal of physical oceanography*, **39,** 1298–1316.
Winant, C. D., 1980: Coastal circulation and wind–induced currents.

Annual Review of Fluid Mechanics, **12,** 271–301.

Xie, L., E. Pallàs–Sanz, Q. Zheng, S. Zhang, X. Zong, X. Yi, and M. Li, 2017: Diagnosis of 3D vertical circulation in the upwelling and frontal zones east of Hainan Island, China. *Journal of Physical Oceanography*, **47,** 755–774.

Yang, H.–W., Y.–K. Cho, G.–H. Seo, S. H. You, and J.–W. Seo, 2014: Interannual variation of the southern limit in the Yellow Sea Bottom Cold Water and its causes. *Journal of Marine Systems*, **139,** 119–127.

Zhang, W. G., G. G. Gawarkiewicz, D. J. McGillicuddy, and J. L. Wilkin, 2011: Climatological mean circulation at the New England shelf break. *Journal of Physical Oceanography*, **41,** 1874–1893.

Zhurbas, V., I. S. Oh, and T. Park, 2006: Formation and decay of a longshore baroclinic jet associated with transient coastal upwelling and downwelling: A numerical study with applications to the Baltic Sea. *Journal of Geophysical Research: Oceans*, **111**.

Zweng, M. M., and Coauthors, 2019: World Ocean Atlas 2018, Volume 2: Salinity. A. Mishonov, Technical Editor. *NOAA Atlas NESDIS*, **82,** 50pp.

Abstract (in Korean)

한반도 남해안에서 바람과 표층 가열의 변화에 대한 해양의 반응에 대해 연구하였다.

2013년 여름 남해안에 전례없는 용승이 발생하였다. 용승은 바람이 멈춘 후에도 약 한 달 가량 지속되었으며 양식장에 큰 피해를 입혔다. 2013년 여름의 용승은 7월 강한 바람에 의해 발생하였고 깊은 수심의 차가운 물을 연안 지역으로 상승시켰다. 연안 지역의 차가운 물은 연안 지역의 해수면을 낮추며 외해와 연안의 압력구배를 크게 하였고 이로 인해 연안을 따라 동쪽으로 흐르는 지형류가 강화되었다. 이렇게 강화된 지형류는 다시 지형류 평형을 통해 깊은 수심의 차가운 물을 연안 지역으로 상승시켰고 이러한 반복 작용으로 인해 바람이 멈춘 후에도 용승이 오래 지속될 수 있었다.

표층 가열이 용승 세기에 미치는 영향을 알아보기 위해 수치 실험을 수행하였다. 용승 세기를 정량적으로 나타내기 위해 외해수송량, 등밀도선 기울기, 그리고 외해와 연안의 수온차이를 계산하였다. 표층 가열은 해양-대기 안정도를 변화시키며 에크만 수송을 감소시키는 한편, 에크만 펌핑을 증가시켰지만 에크만 수송과 에크만 펌핑의 합인 총 외해수송량의 변화는 미미하였다. 표층 가열은 등밀도선 기울기를 완만하게 하고 외해와 연안의 수온차이는 증가시켰다. 등밀도선 기울기와 외해와 연안의 수온차이는 표면경계층의 변화와 큰 관련이

있었다. 강한 표층 가열은 수직와점성계수를 감소시켜서 표면경계층의 두께를 줄이고 표면경계층 내의 외해로 향하는 유속의 세기를 증가시킨다. 총 외해수송량의 변화가 없더라도 얇아진 표면경계층의 두께로 인해 등밀도선의 기울기는 완만해지고 표면경계층 내의 외해로 향하는 빠른 유속으로 인해 외해와 연안의 수온차이는 증가한다.

2019년 남해안의 퇴(bank) 지형에서 바람에 의한 비대칭적 반응이 관측되었다. 외해의 해류를 기준으로 하류보다는 상류쪽에서 연안을 따르는 흐름의 변동성이 더 크게 관측되었다. 이러한 비대칭성의 가장 주요한 원인은 수심 평균 응력에 따라 결정되는 비지균 성분의 움직임이었다. 한편, 퇴 지형에서 연안을 따르는 흐름과 해수면의 분포는 외해의 해류에 크게 영향을 받았다. 외해의 해류가 존재할 때 동풍이 부는 시기에는 퇴 지형의 상류쪽에서 서향류가 오래 지속되고 심지어는 동쪽으로 전파되는 모습을 보였다. 해수면 분포에서는 퇴의 머리 부분에서 최소 해수면의 형태가 나타났다. 반면 서풍이 부는 시기에는 외해의 해류가 연안을 따르는 흐름과 해수면 분포의 비대칭성을 더욱 강화시켰다.